A particle image velocimetry investigation on laboratory surf-zone breaking waves over a sloping beach

Olivier Kimmoun, Hubert Branger

A particle image velocimetry investigation on laboratory surf-zone breaking waves over a sloping beach

O. KIMMOUN[1] AND H. BRANGER[2]

[1]Ecole Centrale de Marseille, Technopôle Château-Gombert, 13451 Marseille, France

[2]IRPHE, CNRS, Aix-Marseille Université, Marseille, France

olivier.kimmoun@ec-marseille.fr; branger@irphe.univ-mrs.fr

Particle image velocimetry (PIV) measurements were performed in a wave tank under water waves propagating and breaking on a 1/15 sloping beach. The wave transformation occurred in the surf zone over a large domain covering several wavelengths from incipient breaking to swash zone beyond the shoreline. PIV spatial interrogation windows must be small enough to obtain accurate velocities, and one window covers only a small part of the domain. To overcome this problem and to measure the instantaneous velocity field over the whole surf zone area, we have split the full field into 14 overlapping smaller windows of the same size. Local measurements were synchronized with each other using pulsed TTL triggers and wave gauge data. The full velocity field was then reconstructed at every time step by gathering the 14 PIV fields. We then measured the complete space–time evolution of the velocity field over the whole surf zone. We determined also the ensemble-period-average and phase-average components of the flow with their associated fluctuating parts. We used the PIV images and velocity measurements to estimate the void fraction in each point of the surf zone. Special attention was given to the calculation of the spatial derivatives in order to obtain relevant information on vorticity and on the physical terms that appear in the fluctuating kinetic energy transport equation.

1. Introduction

Long-term forecast of the coastal shoreline evolution requires high precision of the input terms in morphodynamic numerical models. The hydrodynamic input terms play a dominant role in such modeling; but the internal flow structure in the surf zone is complex, with many intermittent structures at different scales. Wave breaking in depth-limited conditions is one of the most important nearshore processes. Moreover it is difficult to make measurements under breaking waves owing to high accelerations, impacts and air-flow mixing. Previous studies of breaking waves have greatly improved our knowledge of the surf zone, but the present state of the art is still far from satisfactory. So, because of lack of knowledge, people use very simple semi-empirical hydrodynamic models as input for morphodynamic models. To improve the understanding of sediment transport by wave breaking, it is important first to under take experiments that give us the best information on the kinematics and dynamics of wave breaking on beaches. We think it is important to know the evolution of the velocity field, not only at one point in the time domain, but also

in the space–time domain all over the surf zone, from the breaking location to the shoreline. Determination of vorticity, fluctuating kinetic energy, transport of kinetic energy and void fraction are also essential for quantifying physical processes.

Basco (1985), Jansen (1986) and Bonmarin (1989) used photographs to study wave evolution during breaking. Many authors used laser-Doppler velocimetry (LDV) to measure the time evolution of velocities under waves propagating in the surf zone (Ting & Kirby 1994, 1995, 1996; Cox, Kobayashi & Koyabasu 1995; Petti & Longo 2001; Longo 2003; De Serio & Mossa 2006). Hot-film anemometry was also used (Hattori & Aona 1985; Conley & Inman 1992; George, Flick & Guza 1994) to describe the processes of sediment suspension under near-breaking waves, but this technique is intrusive and fragile, so the equipment could be damaged under breaking waves. LDV or hot-film measurements, which allow high-frequency data acquisition rates, are 'point-by-point' techniques, with measurements taken only locally at one point. It does not allow us to have an instantaneous spatial description of the physical phenomena. With LDV, spatial derivatives are estimated through the Taylor hypothesis ($\partial/\partial x = (1/u)\partial/\partial t$). Turbulent energy transport analysis reveals problems associated with the use of the Taylor hypothesis in the surf zone (Ting & Kirby 1995). The Taylor hypothesis states that fluctuations are small compared to the mean flow; this condition is not satisfied in the surf zone since the turbulent velocity fluctuations created by large eddies are not small. Moreover, LDV measurements are usually located under the mean level of the wave troughs and not above them; but Stansby & Feng (2005) succeeded in making LDV measurements above the trough level. During the last decade, instantaneous spatial velocity measurements have been conducted using particle image velocimetry (PIV) (see Adrian 1991 for a review). PIV provides improved spatio-temporal coverage. This technique has, however, some limitations, owing to low-frequency image acquisition, and to the relatively poor accuracy of the velocity measurement, with many additional residual errors due to camera resolution, light reflection by bubbles, seeding inhomogeneity, loss of two-dimensionality, etc. PIV measurements under wave breakers were first investigated for deep-water waves (Lin & Rockwell 1994, 1995; Dabiri & Gharib 1997; Melville, Veron & White 2002), then for shallow-water waves (Chang & Liu (1998, 1999)), and also for waves breaking over a submerged obstacle (Chang, Hsu & Liu 2001, 2005).

Peregrine (1983) and Battjes (1988) made a complete review of the hydrodynamics of the surf zone. They described breaking mechanisms of waves breaking on sloping beaches. Nadaoka, Kino & Koyano (1989), in wave tank experiments for spilling breakers, observed large oblique vortex structures with descending trajectories that seem to play a dominant role in the mass transportation. Large horizontal vortices were also observed by Cox & Anderson (2001). Ting & Kirby (1994, 1995, 1996) and Ting (2001) performed experiments in order to study kinetic turbulent transportation in the surf zone under waves breaking over a 1/35 sloping beach. They showed that fluctuating kinetic energy is transported shoreward by plunging breakers and seaward by spilling breakers. As Stansby & Feng (2005) noted: 'This could be associated with turbulence being more concentrated in the roller for plunging breakers with prominent shoreward motion and being more distributed for spilling bores'. They also found that the characteristic length scale linked to turbulent transport is of approximately the same order as the wavelength. Their measurements were made only between the bottom and the mean level of the wave troughs. With LDV measurements, Cox & Kobayashi (2000) showed that intense, intermittent events exist in the surf zone in the case of regular spilling waves over a 1/35 slope beach. These events are not always correlated with the passing of each wave. Petti & Longo (2001) measured turbulent

velocities and waterfront dynamics in the swash zone over a 1/10 slope beach. They showed that turbulent energy was higher during uprush than during backrush. Their measured energy flux was essentially directed shoreward. Stansby & Feng (2005) found multiple vortical structures at the initiation of breaking, becoming elongated along the surface during the bore propagation. With period average kinematics, they showed a shoreward mass transport above trough level and undertow below. De Serio & Mossa (2006) measured the Reynolds shear distribution in the shoaling zone, the maximum values being located under the crests.

The PIV results clearly showed high vorticity production by breaking; but for shallow-water waves, the vertical mixing layer is restricted vertically. For waves propagating and breaking over a flat bottom, Chang & Liu (1998, 1999) found that vorticity was of the same magnitude as wave phase speed divided by water depth. The maximum turbulence intensity outside the region aerated by bubbles was one tenth of the phase speed. Cox & Anderson (2001) performed PIV measurements in the horizontal plane under breaking waves. Their PIV interrogation window was only $10 \times 10\,\mathrm{cm}^2$, but they found intermittent horizontal coherent structures near the seaward face of the breaking crests. Govender, Mocke & Alport (2002) studied waves breaking over a 1/20 sloping beach for spilling and plunging breakers. They used a new technique (digital correlation image velocimetry, DCIV) with the analysis of bubble structures in the foam region to retrieve the velocity in the breaker. They showed that turbulence generation occurred under the forward wave and that turbulence is moved downward. They also showed that the onshore mass transport above the mean water level is greater than the offshore mass transport under the mean water level. This non-equilibrium results from the density of the foam region not being taken into account. Cowen *et al.* (2003) measured turbulent Reynolds stresses in the swash zone using PIV and showed that flow forced by plunging and spilling breakers are similar. The uprush and downrush phases are not symmetric: the uprush is dominated by bore-advected turbulence, and the downrush is much less turbulent.

The main differences between the present paper and previous studies are the surf zone full-field reconstruction from different PIV windows, the space-phase-averaged presentation and a map of the void fraction covering all the surf zone. Experiments were conducted in the EGIM/ECM wave tank in Marseille. We made PIV velocity measurements under regular waves breaking on a 1/15 sloping beach. We measured velocities even in the vicinity of dual-phase air–water aeration. We made synchronized space–time measurements in 14 locations along the surf zone. Then we gathered together local data and merged them to produce a space–time full field coverage of the whole surf zone. We computed mean and fluctuating parts, ensemble-average statistics, and also spatial phase-average decomposition with their associated mean and fluctuating parts. The experimental set-up is described in § 2. We show some data validation in § 3. Instantaneous local and global velocity fields are displayed in § 4. Ensemble average (§ 5), aeration (§ 6) and phase average (§ 7) results are presented. In § 8, we quantify phase-locked fluctuating velocity components, fluctuating kinetic energy and the associated production, dissipation and advection terms that appear in the fluctuating kinetic energy transport equation. Conclusions are drawn in § 9.

2. Experimental set-up

Experiments were conducted in the EGIM/ECM wave tank in Marseilles. A side view of the tank with the experimental set-up is shown in figure 1. The glass-windowed tank is 17 m long and 0.65 m width. The water depth in front of the wavemaker is

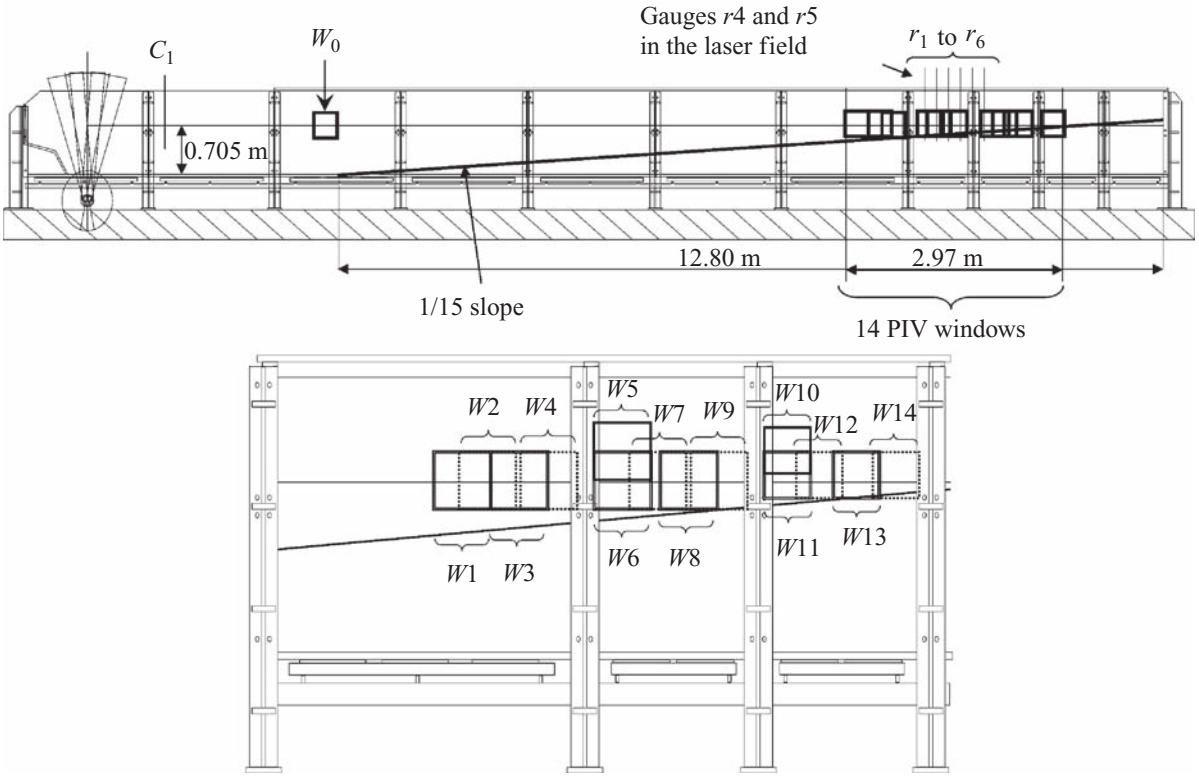

FIGURE 1. Side view of the experimental set-up.

about 0.705 m. A polyvinyl 1/15 sloping beach was mounted on the bottom. The beach, which is about 13 m long, is partly made with transparent glass in order to let the laser light sheet cross the beach vertically from the bottom to the free surface. The transparent glass and the laser sheet are placed at 18 cm from the right-hand side of the wave tank. The toe of the beach is 4 m away from the wavemaker. The rigidity of the beach is ensured by transverse vertical plates spaced every 1 m, by longitudinal plates between the vertical plates and by the thickness of the beach plates (=2 cm). The beach is screwed onto the vertical plates. The maximal vertical displacement of the beach, observed during experiments was less than 1 mm. Because of the vertical PVC plates, which were located under the beach to ensure rigidity, it was not possible to put the vertical laser sheet in the centre of the tank. Transverse perturbations away from the centreline are evaluated in § 3, figure 7. To characterize the wave field, water elevation was measured with a set of six regularly spaced resistive wave gauges, with a distance of 18 cm between each pair of gauges. Several runs allow us to displace on a rail system this set of gauges all along the tank from the wavemaker up to the breaking region. The space evolution of the maximum, the minimum and the mean water level are shown in figure 2. We see clearly the wave shoaling, the crest/trough asymmetry and the mean water level set-up. During the PIV experiment, this set of gauges and the video camera were mounted on the same optical rail system, allowing us to translate horizontally the whole experimental set-up (see figure 3). With this moving set-up, the same two wave gauges were always in the visualization area of the camera. The wave data acquisition frequency was 200 Hz.

The velocity field in the water was measured with a PIV technique (see Adrian 1991 for a complete review). The PIV equipment is shown in figure 3. The water was seeded with 6 μm diameter silver coated hollow glass spheres with a density of around 1.1 g cm^{-3}. Their free vertical fall speed was negligible ($\ll 1$ mm s^{-1}). A twin ND-Yag pulsed laser (2×300 mJ) produced a stroboscopic light sheet through a hinged arm

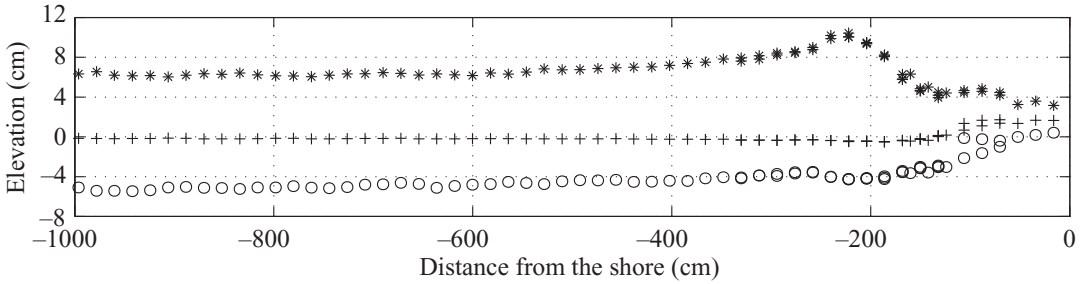

FIGURE 2. Wave properties along the beach measured with the wave gauges: o, trough; +, mean sea level; *, crest.

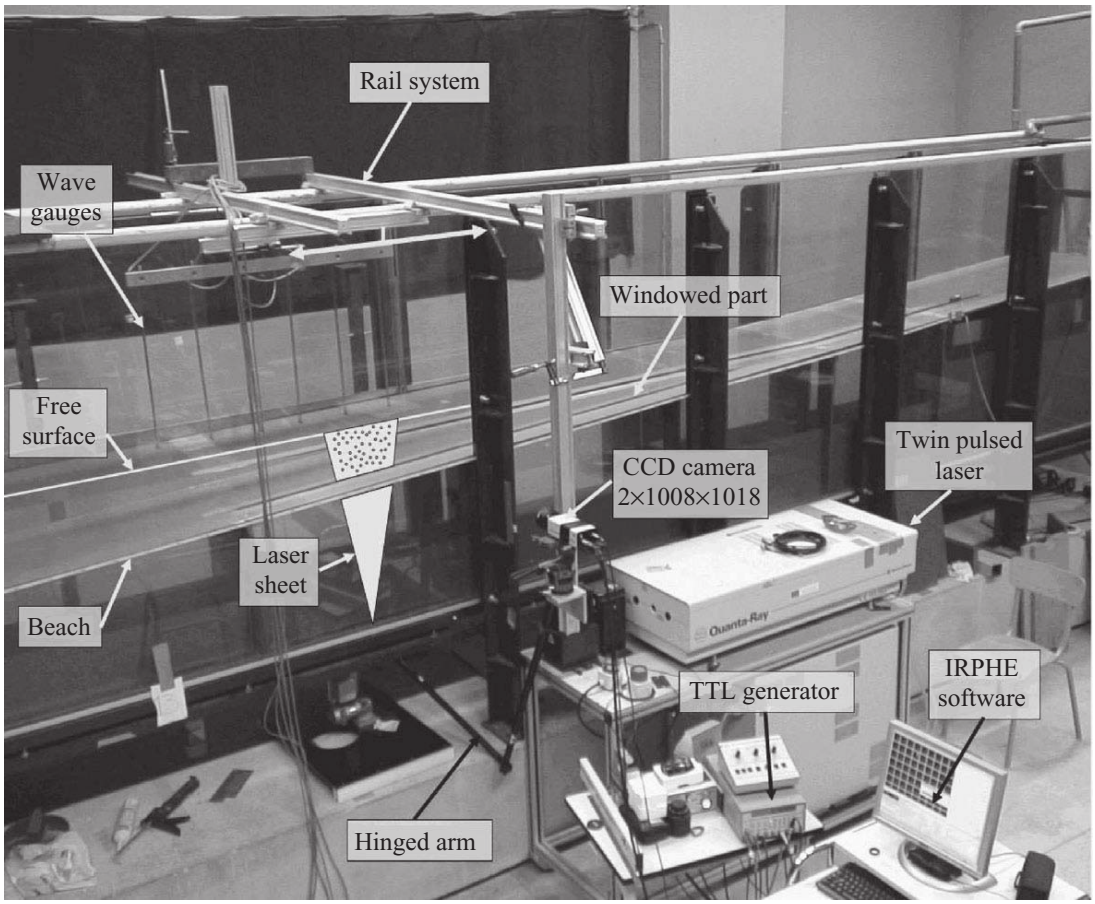

FIGURE 3. PIV apparatus.

equipped with optical lenses. Pairs of images were taken with a double CCD-frame camera, with a resolution of 1008×1018 pixels and 256 grey intensity levels. Image data acquisition was synchronized with the laser pulses. We took a pair of images every $\Delta t = 100\,\text{ms}$, so we had 10 instantaneous velocity fields per second. The time delay between a pair of images was 7 ms. To compute the velocity field from the digitized particle images, we used a recursive intercorrelation interrogation window technique with several loops, taking into account pre-computed velocity gradients and vorticity (Westerweel, Daribi & Gharib 1997; Meunier & Leweke 2003). For the first loop, the interrogation window size was 64×64 pixels, then for the second and the subsequent passes we used a smaller window (32×32 pixels) because the motion was contained by the window shift. To avoid sub-pixel locking, we used a Gaussian filter of size 3 (Westerweel 1993). Particular care was given to the automatic water elevation surface profile detection. The pixels located in air are darker than the pixels

Window	Position (cm)	Size (cm^2)	Overlap (%)	Window	Position (cm)	Size (cm^2)	Overlap (%)
w1	−258	37×37	×	w8	−118	37×37	49
w2	−242	37×37	56	w9	−106	37×37	67
w3	−223	37×37	48	w10	−72	37×37	11
w4	−203	37×37	50	w11	−60	31×31	58
w5	−172	37×37	16	w12	−37	31×31	26
w6	−159	37×37	66	w13	−15	31×31	26
w7	−137	37×37	40	w14	+7	31×31	31

TABLE 1. For each window: horizontal distance from the window centre to the shoreline, window size and overlapping between adjacent windows.

located in water. The automatic surface contour detection is a gradient grey-level detection with a threshold value computed from the probability density function of grey intensity levels. For each image, the detected water elevation profile was used to build a mask to invalidate all the velocity vectors located in air: the pixels in air were set to 256 (white is 255) and any cell that contained a pixel with this value was not considered in the PIV calculation (Kimmoun, Branger & Zucchini 2004). Similarly, a mask with a 256-level value was added under the beach. In the foam generated during the breaking event, seeds were not clearly visible, so then, the PIV intercorrelation algorithm was not really based on particle displacements, but more on micro-foam structure and bubble displacements, as explained in Govender (1999) and Govender *et al.* (2002). Briefly, the position of the peak in the cross-correlation of PIV interrogation windows provides a measure of the displacement of the structure created by the air bubbles during wave breaking.

In this paper, the vertical coordinate z is measured positive upward from the still-water level, the horizontal coordinate x is measured negative seaward from the shoreline at rest, $\eta(x, t)$ is the instantaneous surface elevation, $d(x)$ is the local still-water depth, $\bar{\eta}(x)$ is the mean sea level and $D(x) = d(x) + \bar{\eta}(x)$ is the local mean water depth (referred to as D).

In this experiment, the length of the surf zone was about 3 m. In order to retrieve the full velocity field all along this distance, we made camera PIV measurements in 14 locations ranging from the incipient breaking location to the swash zone. The location of these 14 interrogation windows is shown in figure 1, and for each window, the position, the size and the overlapping is given in table 1. For windows w1 to w10, the size of the PIV images was 37×37 cm^2 which corresponds to a resolution of 0.037 cm/pixel, and for windows w11 to w14, where the depth was small, the size of the PIV images was reduced to $31 \times 31\,cm^2$, which corresponds to a resolution of 0.031 cm/pixel. The video PIV experimental set-up (camera, light sheet) and the wave gauge set-up were moved successively to each individual window location. For windows w5 and w10, the depth in front of the wavemaker was increased by 1 cm in order to obtain information behind the post of the wavetank. Owing to the 1/15 beach slope, a 1 cm vertical increase of water depth in the canal was equivalent to a 15 cm horizontal shift to the left. Wave gauge data allow us to verify the matching between the free surface recorded at a position x and the free surface recorded at a position $x + 15\,cm$ with a water depth set-up of 1 cm. Our goal was to build instantaneous full velocity fields by combining local instantaneous results from the 14 PIV window acquisitions. To achieve this, we synchronized PIV image acquisition and wave gauge

data using an impulse TTL generator (Digital Delay Generator DG535 from Stanford Research Systems). We used the same time triggers and duration acquisitions for all experiments. Repeated experiments were conducted using the same wavemaker signal and TTL pulse delivery. This overall synchronization allowed us to reconstruct, at each time step, a full velocity field covering the entire surf zone, as explained in detail in § 4.

Other PIV measurements were made between the wavemaker and the beginning of the sloping beach, where the bottom is flat. We used these data to characterize the incipient waves and to validate PIV measurements by comparing results with theoretical developments.

Such experimental measurements and analysis are time consuming and only one paddle wave condition was generated and analysed in this experiment. While breaking wave dynamics depends highly on the incipient wave characteristics, the results presented here will provide a general qualitative assessment of the flow structures and properties during wave shoaling and breaking on a beach. Most of the results in the following sections will be presented in a non-dimensional form for a better comparison with previous experiments in the literature. The quantitative evaluation for one case would help in analysing further more complex situations. In this experiment, the wave period was $T = 1.275$ s, and wave amplitude before the sloping beach at depth $d = 70.5$ cm ($d = 71.5$ cm for w5 and w10) was $a = 5.7$ cm. The wavemaker motion for regular wave generation is sinusoidal. The wavelength at this location was $L_0 = 2.41$ m. The wave height at breaking was $H_b = 14$ cm. This measured wave height fits very well the theoretical value given by Miche (1951): $H_b = 0.14\, L_0 \tanh(2\pi D/L_0) = 13.9$ cm. The surf similarity parameter was $\zeta = S/\sqrt{H_b/L_0} = 0.28$, with S the beach slope. This value usually characterizes a spilling breaker (Battjes 1988; Ting & Kirby 1995, 1996). The wave reflection coefficient was measured in the flat part of the wave tank and was less then 2 % in amplitude (the six wave gauges were moved to the flat bottom part for this measurement). For each camera position, two runs with the same wavemaker conditions were done. We waited a sufficiently long time (30 min), before starting a new run. Then, for each new run, we waited a statistical quasi-stationary sea-state (128 first wave-cycles) before starting data acquisition. Image acquisition duration was set to 163.2s corresponding to 128 wave periods (wave-cycles 129 to 256). Finally, a total number of $n = 14 \times 1632 \times 2 = 45\,696$ couples of images were acquired and processed.

Figure 4 is an example of the breaking process observed during the experiment in the different PIV windows. Breaking appears first on the very top of the crest (w2 and w3). The foam is very thin. The waves broke initially at about $x \simeq -250$ cm from the shoreline. Rapidly, the breaking turns to be temporarily plunging with an overturning lip (w4). A first splash-up is generated when the lip hits the water surface in front of the wave (w5). There is a growth of a large amount of mixed air–water area with foam, bubbles and whitecapping. The wedge of water pushed up by the plunging jet forms another splash-up jet which strikes the water ahead of it at a second plunging point (w7). The wavefront moves into a roller propagating towards the shore (w8 to w11). The volume of mixed air–water decreases gradually. The wave crosses the shoreline (w14) and the flow runs up before coming back.

3. Measurement validation

The PIV technique is now a well known and commonly used tool to measure velocity field in fluids (Lin & Rockwell 1994; Perlin, Bernal & He 1996; Skyner 1996;

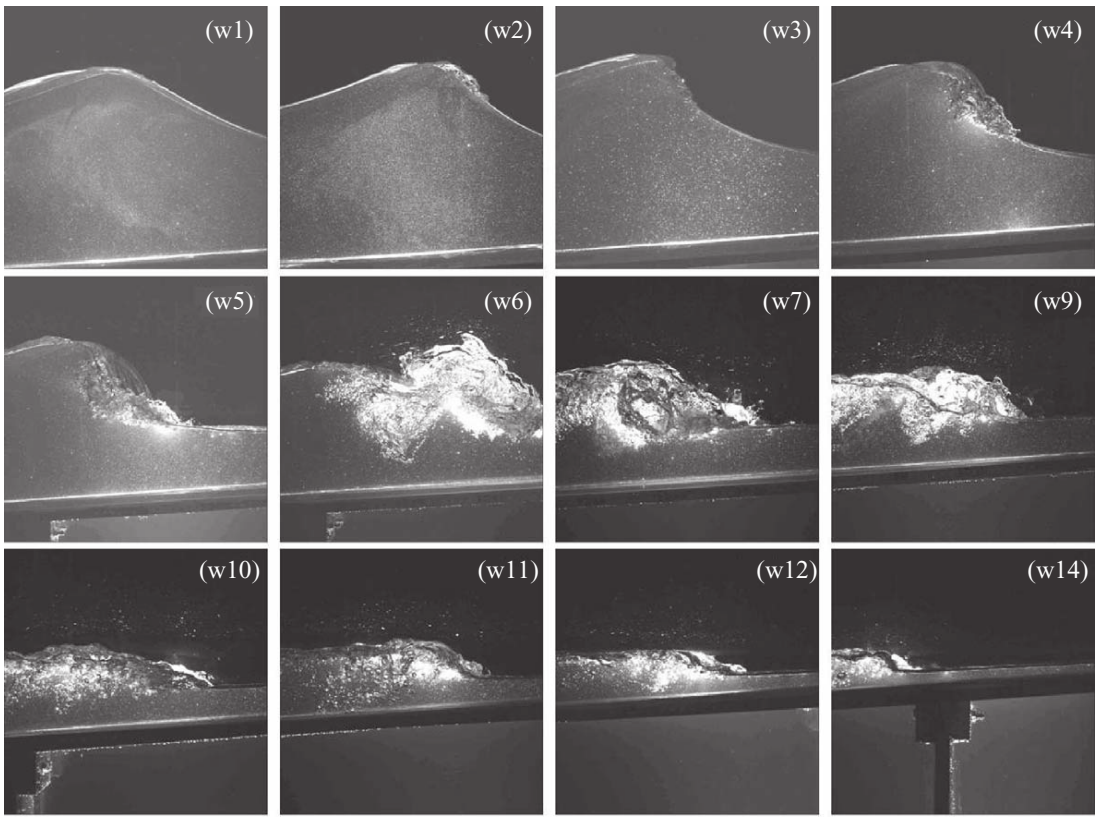

FIGURE 4. Example of a wave breaking event as it appears on overlapping PIV interrogation windows.

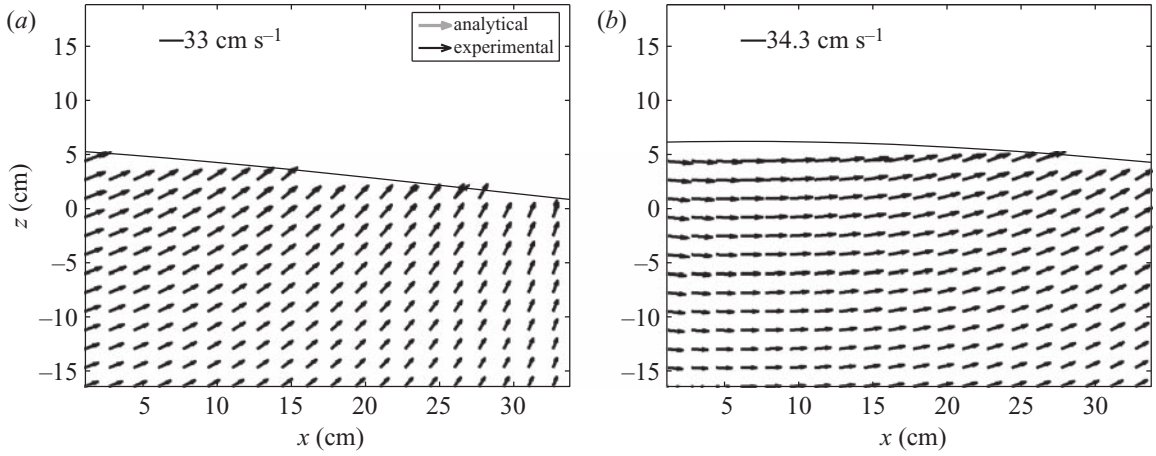

FIGURE 5. Analytical (Fenton 1985) versus experimental comparison at window location w0 of figure 1 at two different wave phases. (*a*) Mean relative velocity error $\overline{\epsilon}_{r,velocity} = 5.6\,\%$, mean absolute direction error $\overline{\epsilon}_{a,direction} = 1.7°$; (*b*) $\overline{\epsilon}_{r,velocity} = 7.0\,\%$, $\overline{\epsilon}_{a,direction} = 1.7°$.

Dabiri & Gharib 1997; Peirson 1997; Govender *et al.* 2002; Melville *et al.* 2002). The PIV equipment and the software developed at the IRPHE laboratory have been used and validated for several physical applications (Meunier & Leweke 2003). In order to validate the PIV apparatus for our experimental arrangement, we have measured the velocity field under regular waves propagating over the flat part of the bottom of the tank (window w0 in figure 1) and compared the results with a fifth-order analytical solution (Fenton 1985). Two examples of experimental/analytical comparisons are shown in figure 5 at two different wave phases. Differences between experimental measurements and analytical results are weak. The mean relative error for the flow

velocity over the whole domain for a full wave period is equal to $\overline{\epsilon}_{r,velocity} = 7.2\,\%$, with $\overline{\epsilon}_{r,velocity} = \overline{\|\boldsymbol{u}_{Measured} - \boldsymbol{u}_{Analytical}\|/\|\boldsymbol{u}_{Analytical}\|}$. The mean absolute error for flow direction is $\overline{\epsilon}_{a,direction} = 3.8^{\circ}$, with $\overline{\epsilon}_{a,direction} = \overline{|\arg(\boldsymbol{u}_{Measured}) - \arg(\boldsymbol{u}_{Analitycal})|}$. This comparison shows the ability of our PIV apparatus and software to measure velocities under regular waves, even near the free surface.

It was not possible to validate PIV measurements in the breaking zone because there is no analytical solution to compare with. Available numerical simulations have to be validated and thus cannot be taken as a reference.

Comparisons with previous experiments published in the literature can be made with non-dimensional values, because the input experimental parameters are not exactly the same. To evaluate our ability to measure velocities in the breaking region, we will compare in the following sections, in a non-dimensional form, our global PIV velocity fields and fluctuations with some of the known published LDV or PIV results cited in § 1. Here, the main differences from previous studies are the surf zone full-field reconstruction from different PIV windows, the space-phase-averaged presentation (see following sections), and the presentation of a map of the void fraction covering all the surf zone. We used the same algorithm for velocity determination in the whole surf and swash zones. We used two criteria to detect spurious velocity vectors: (i) intercorrelation peak detection criterion: the height of the highest peak of the intercorrelation between two interrogation windows should be greater than 1.2 times the secondary peak (Adrian 1991); (ii) average median criterion: the velocity vector should not differ by more than 50 % in modulus and $\pi/6$ in direction from the median value of all the neighbouring vectors (Meunier & Leweke 2003). Then, spurious vectors are replaced by a median-filter procedure (see Westerweel 1994 for details).

In order to validate our automatic surface contour detection (see § 2), we have compared water elevation measured by wave gauges with the water surface level computed from PIV images. Figure 6 gives three examples of time series comparisons at three different stages of breaking. Differences are weak during incipient breaking (figure 6*a*, window w1 of figure 4), and roller phase (figure 6*c*, w12). Differences appear during the plunging and splash-up events (figure 6*b*, w7). During these events characterized by a large air entrainment, the resistive wave gauge response is proportional to the wire wet length which is lower than the actual surface elevation, as shown in figure 4 (figure 6*b*). The relative root mean square (r.m.s.) difference between gauges and PIV measurements is displayed in figure 4 (figure 6*d*). This difference is related to the void fraction. This point will be discussed in § 6.

Even if the wave tank is narrow in comparison with the wavelength of the regular waves we generated, it is necessary to verify the two-dimensionality of the mean flow. For this purpose we measured at 12 positions from the wavemaker, the surface elevation for three transverse positions: at 18 cm from the right-hand side of the tank, at the centre and at 18 cm from the left-hand side of the tank. For each wave gauge time series ($t \in [129T, 256T]$), we extracted 128 waves by a zero up-crossing analysis and we computed a time-phase average profile. In figure 7(*a*), we displayed the relative root mean square error between the left/right time-phase average profile and the centre time-phase average profile. Values are smaller than 10 %, so they characterize a good two-dimensionality of our mean wave profile from incipient breaking to the end of the first splash-up. An example of time-phase average profiles at the three transverse positions is given in figure 7(*b*) at a distance from the shoreline of $x = -186$ cm, at the end of the plunging phase. Clearly, there is good two-dimensionality near the wave crest, with some discrepancies near the troughs.

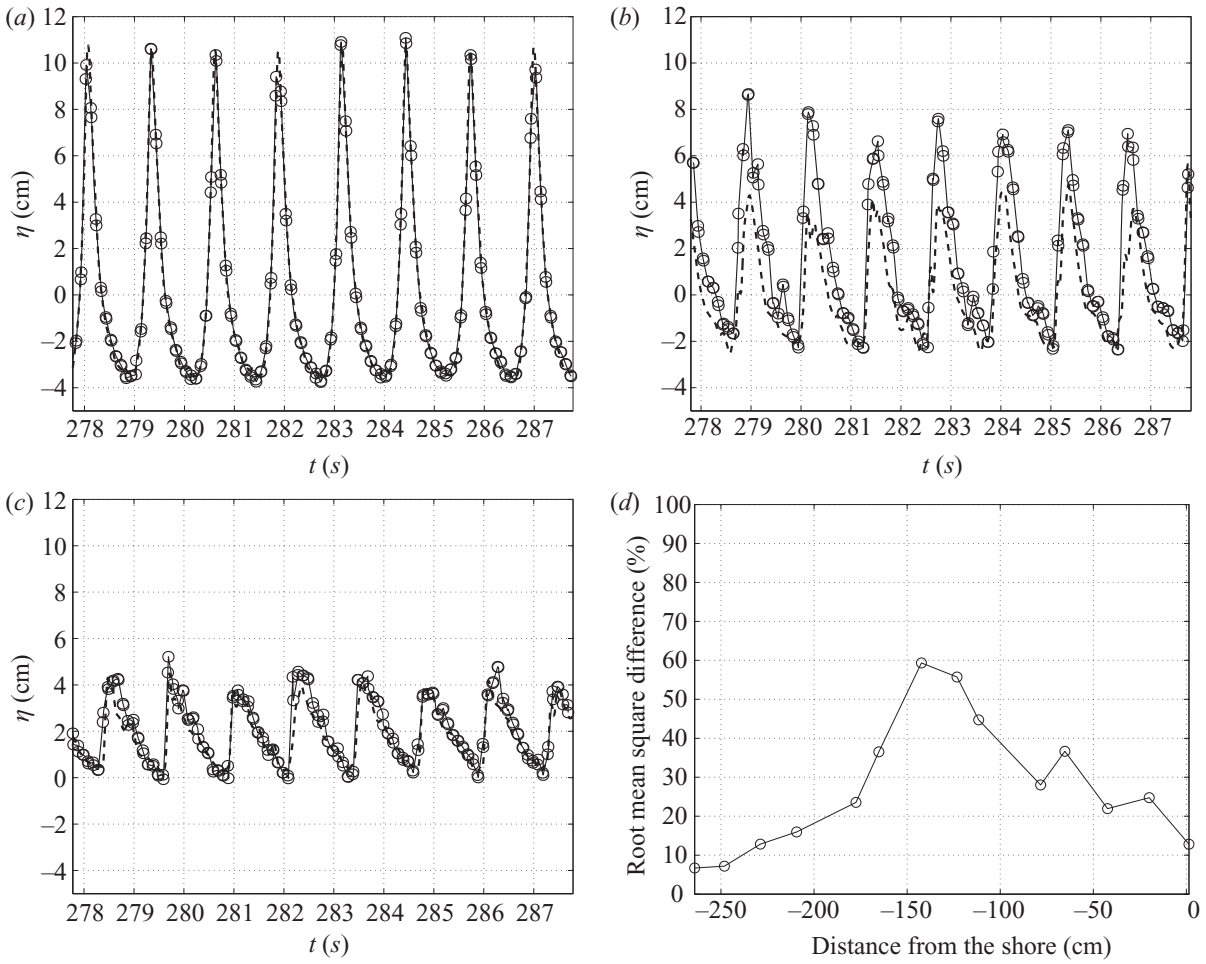

FIGURE 6. Time series comparison between wave gauge elevation (dashed lines) and automatic surface detection from PIV images (circles). Distance from shoreline: (*a*) 248 cm (incipient breaking), (*b*) 142 cm (splash-up event), (*c*) 42 cm (roller). (*d*) r.m.s. difference (%) between the PIV surface detection and the wave gauge measurements.

In order to describe the uncertainty in our turbulence measurements and to describe how the error measurements propagate into our estimates of higher-order turbulence quantities (see § 8 for fluctuating velocities and higher-order fluctuating component determination) we performed a bootstrap analysis and calculated the uncertainty interval at the 95 % confidence level for the different fluctuating quantities (Efron & Tibshirani 1993; Zoubir & Boashash 1998). Figure 8 shows some examples of the evolution of uncertainty intervals at the 95 % confidence level for some random components. The depth-average of the uncertainty intervals for $\sqrt{u'^2}$, $\sqrt{w'^2}$, Reynolds stress ($u'w'$) and one term of the kinetic energy production formulation: $u'^2(\partial U/\partial x)$ are displayed in figure 8 for different distances from the shoreline and for phase $\varphi = 106^\circ$ (see §§ 7 and 8 for notation, phase and fluctuating components determination). Typical uncertainty intervals were found to be around 12 % for fluctuating velocities, around 20 % for Reynolds stress, and around 25 % for higher-order components. We observe some higher localized values (*a*) near the shoreline ($x > -40$ cm) because the turbulence level is high and the PIV measurements are less precise during the down-rush phase in this area (see figure 15 and the discussion at the end of § 5 before (5.3)); and (*b*) far from the shore ($x < -250$ cm), where the turbulence level is very low, thus giving a large 'relative' error because the corresponding 'mean' value in the

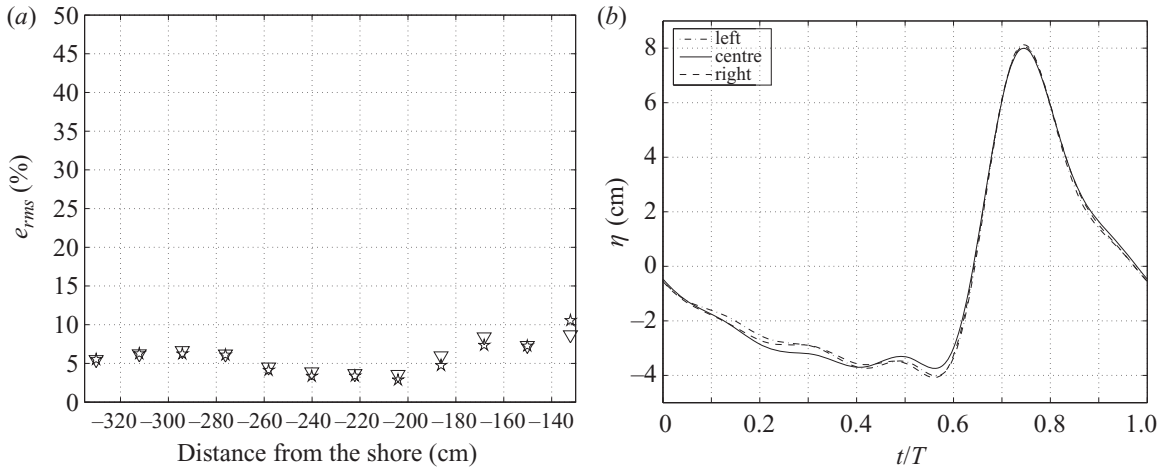

FIGURE 7. (*a*) Relative r.m.s difference between the mean profile at 18 cm from the left-hand side of the tank (star) and at 18 cm from the right-hand side (triangle) to the profile at the middle of the tank. (*b*) Mean profiles at the three transverse wave gauge positions at a distance from the shoreline of $x = -186$ cm.

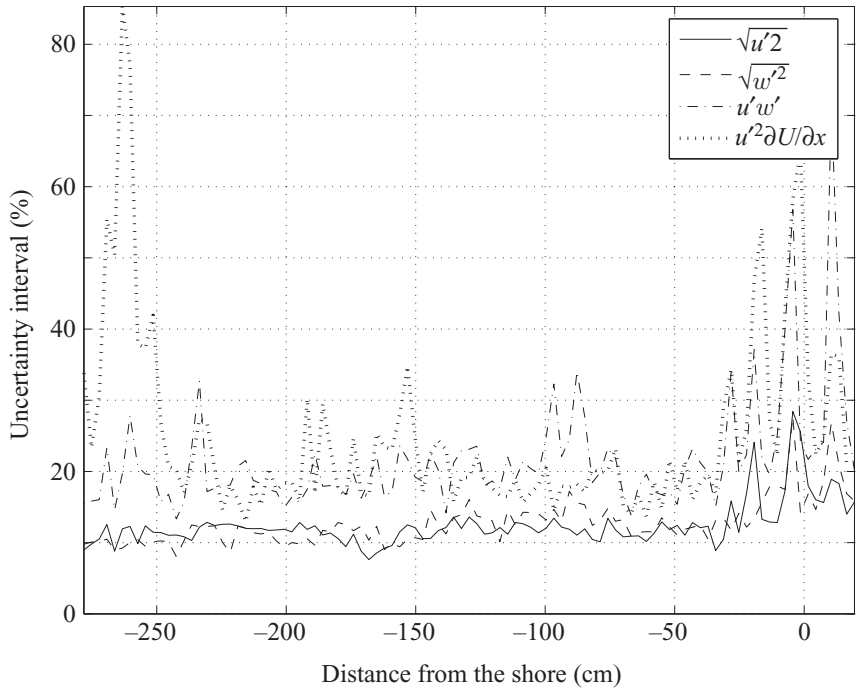

FIGURE 8. Examples of uncertainty intervals at the 95 % confidence level using the bootstrap method for random components (Efron & Tibshirani 1993; Zoubir & Boashash 1998). The x-axis is the distance from the shore. We present the vertically integrated mean of the uncertainty intervals at the 95 % confidence level for fluctuating velocities $\sqrt{u'^2}$, $\sqrt{w'^2}$, Reynolds stress ($u'w'$), and one term of the kinetic energy production term: $u'^2\partial U/\partial x$. These results are for phase $\varphi = 106°$ (see § 7 and 8 notation and determination of for phase and fluctuating quantities).

denominator is low. We found quantitatively similar results at different wave-phase for different fluctuating terms.

The error measurements do not propagate into our estimates of higher-order turbulence quantities because we used cubic smoothing spline interpolation to construct the velocity field over the whole surf zone (cf. § 4). A major asset of the spline function is the direct use of calculated spline coefficients to compute

space-derivative $\partial/\partial x$ and $\partial/\partial z$, without noise contamination (Spedding & Rignot 1993; Fouras & Soria 1999; Cohn & Koochesfahani 2000). With this technique, we avoid the use of the first-order difference scheme, therefore the quantities calculated with derivatives are calculated with the same spatial discretization as terms without derivatives. In conclusion, the uncertainty intervals at the 95 % confidence level for higher-order fluctuating quantities are on average lower than 30 %, but with some localized exceptions.

4. Instantaneous velocity field and full field reconstruction

Examples of instantaneous PIV velocity field are shown in figure 9. They correspond to the mosaic of PIV images shown in figure 4. In each figure, the two surface profiles automatically detected from PIV image couples are displayed. These figures show clearly the ability of the PIV algorithm to measure velocities directly from raw images, even in the mixed air–water region.

The surf zone is about 3 m long. Because of lack of resolution, it was not possible to measure the full velocity field over the entire surf zone with only one PIV 1018×1008 pixels observation window. As explained in § 2, at each time step, we measured the velocities at 14 locations ranging from the incipient breaking area to the swash zone (figure 1). We built an instantaneous full velocity field by combining the 14 instantaneous results. Such a mosaic technique was used by Melville *et al.* (2002) for wave breaking in deep water. Synchronization was done using pre-defined impulse TTL signals. The first TTL pulse started wave gauge data acquisition and the wavemaker simultaneously, and the second one, 163.2 s (128 wave periods) later, started the PIV image acquisition. This technique allows us to obtain a 1 ms precision (electronic precision of the TTL generator) on the synchronization between the different runs. The run-to-run repeatability has been estimated by computing the water elevation phase-to-phase variation between the different runs. For the wave gauge located in front of the wavemaker, the standard deviation of the phase, computed by fast Fourier transform-analysis, between the 28 runs (two runs per window) was found to be 0.94°. An example of gathering the mosaic of raw images at a given instant is given in figure 10. Overlapping between windows shows clearly the good continuity between adjacent fields. In order to build a continuous global field over the whole surf zone, we first computed a continuous water surface profile by interpolating the 14 local wave profiles using cubic spline interpolation. Then we defined a new non-homogeneous space grid, $(x_i, z_{i,j})_{i=1,\ldots,504,\, j=1,\ldots,324}$, over the full domain, as follows: abscissa x_i are regularly distributed in the x-direction along the surf zone from $x_1 \simeq -280$ cm, up to $x_{504} \simeq +21$ cm ($\Delta_x = 0.592$ cm), and, for each abscissa x_i, points $(x_i, z_{i,j=1,\ldots,324})$ are regularly distributed in the z-direction from the local bottom location, $z_{i,1} = -d(x_i)$, up to the local surface water elevation, $z_{i,324} = \eta_i$. From the 14 original groups of raw data, horizontal and vertical components of velocity vectors were then interpolated on this new grid. We used a cubic smoothing spline interpolation routine, with a smoothing parameter $p = 0.5$ (De Boor 1978). The influence of the smoothing parameter will be discussed in § 8. The final velocity field reconstructed from the mosaic of figure 10 is shown in figure 11. Velocities and water profile are now a continuous function of space, with no gap between the data. We reconstructed a total set of $n_r \times n_c \times T \times n_a = 3264$ different velocity fields and wave profiles over the surf zone, with $n_r = 2$ (2 runs per window), $n_c = 128$ (128 wave cycles), $T = 1.275$ s (wave period), and $n_a = 10$ (PIV acquisition rate per second).

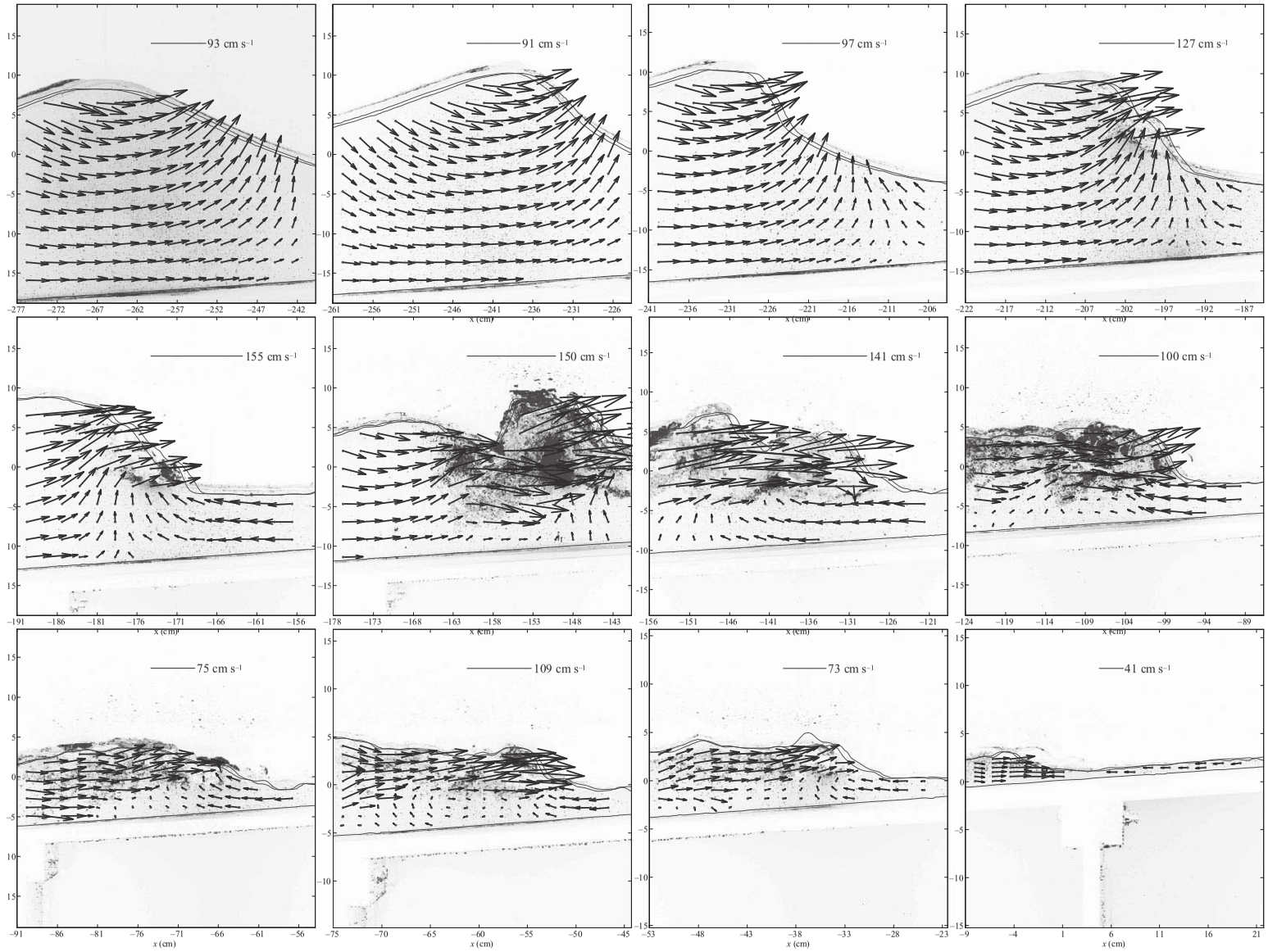

FIGURE 9. Examples of instantaneous PIV velocity fields: results for the mosaic of PIV images displayed in figure 4.

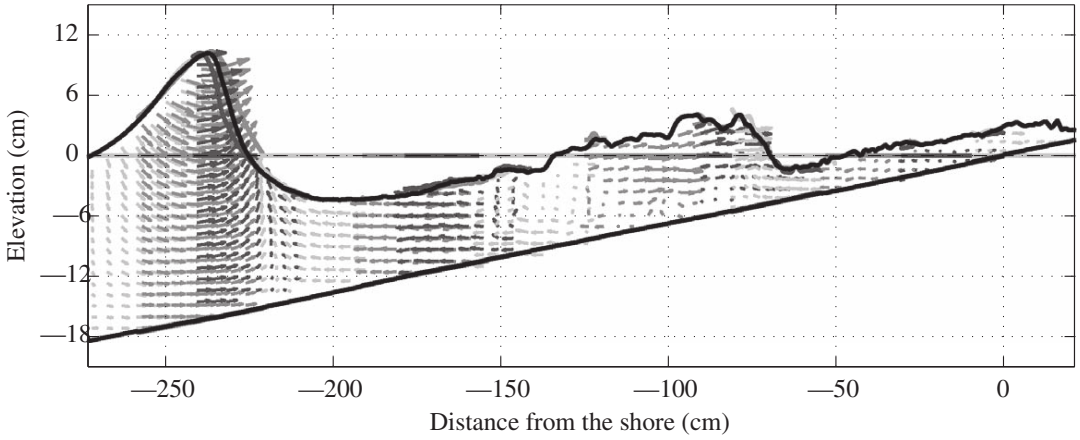

FIGURE 10. Mosaic of velocity fields at a given instant, before reconstruction (only 1/8 of the arrows are displayed in the x-direction and 1/2 in the y-direction).

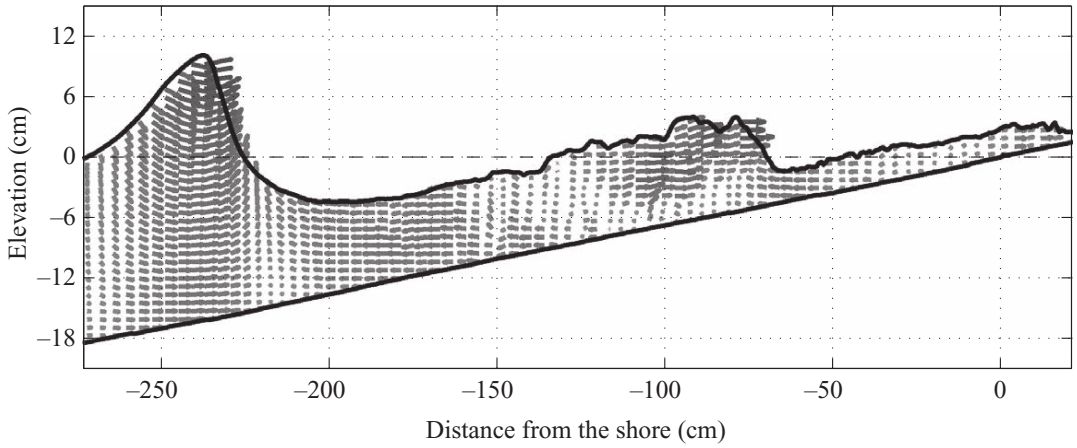

FIGURE 11. Reconstructed and interpolated full velocity field (only 1/6 of the arrows are displayed in the x-direction and 1/12 in the y-direction).

5. Ensemble average

The 3264 different velocity fields over the surf zone finally represent 256 different wave cycles. We first calculated the time-averaged mean flow velocity field by averaging all data. When a wave is propagating shoreward, the points located between the troughs and the crests are alternately in the water and in the air depending upon the local wave phase. A zero velocity value in air should not be considered for averaging. So, we decided to take the ensemble-time-averaged mean value as:

$$\overline{\boldsymbol{U}}(x,z) = \int_0^{nT} \delta(x,z,t)\boldsymbol{U}(x,z,t)\,\mathrm{d}t \;\Big/\; \int_0^{nT} \delta(x,z,t)\,\mathrm{d}t, \tag{5.1}$$

with $n = 256$ and $\delta(x,z,t)$ set to, respectively, 1 when the point (x,z) is located, at instant time t, in water and 0 if the point is located in air. A map of the horizontal component of the non-dimensional velocity $\overline{\boldsymbol{U}}(x,z)/\sqrt{gD(x)}$ is presented in figure 12. $\sqrt{gD(x)}$ is a first-order approximation of the wave celerity at depth $D(x)$. In this figure, we have also plotted $\bar{\eta}_{Max}(x)$ the crest-envelope (locations of the wave maxima), $\bar{\eta}_{min}(x)$ the trough-envelope (locations of the wave minima), and $\bar{\eta}(x)$ the mean water level. They were computed from the 3264 different water surface elevation profiles. Downward arrows in figure 12 show the locations of the beginning of the main

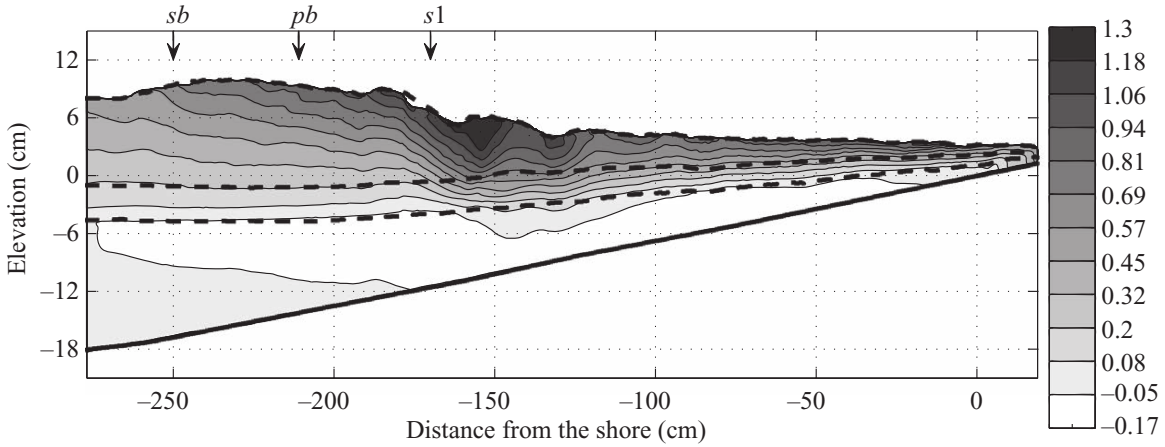

FIGURE 12. Map of the non-dimensional ensemble-time-averaged velocity field, $\overline{\boldsymbol{U}}(x,z)/\sqrt{gD(x)}$ (horizontal component). Dashed lines: crest-envelope $\bar{\eta}_{Max}(x)$, mean water level $\bar{\eta}(x)$ and trough-envelope $\bar{\eta}_{min}(x)$.

events: beginning of breaking ($\downarrow sb$), beginning of plunging ($\downarrow pb$) and beginning of the first splash-up ($\downarrow s1$).

The set-up of the crest-envelope after the initial break-point ($\downarrow sb$) is comparable with other experiments (Madsen, Sovensen & Shaffer 1997; Stansby & Feng 2005). The mean water level increases after breaking, as has been observed in many experiments (Battjes 1988; Cox *et al.* 1995; Mocke 2001; Petti & Longo 2001; Govender *et al.* 2002). We observe the two bumps on the crest-envelope and mean sea level observed for longer waves by Stansby & Feng (2005) after the plunging event, but in our case they were less pronounced. This is due to the smaller similarity surf parameter in our case. Amplitudes of wave crests are much higher than amplitudes of wave troughs during wave breaking, leading to the well-known horizontal crest-to-trough asymmetry. Figure 12 shows that mean velocities are directed onshore above the trough-envelope and offshore under this line. Mean positive velocities (shoreward) appear to be much greater than negative velocities. Maximal intensities, which were nearly 33 % higher than unity in the non-dimensional form, occur at the crests during the splashing event. This value is close to maximum celerities found by Stansby & Feng (2005) (table 1) in their experiment. Owing to PIV elementary box-size resolution, we were not able to measure velocities exactly at wave crest, but at half elementary box-size (0.59 cm) below it. Near the bottom, maximum reverse non-dimensional velocities reach $0.17\sqrt{gD}$. Ting & Kirby (1995) found similar values with LDV measurements.

The mean velocity values computed above the trough envelope do not have a concrete physical meaning, because the physical points are not always located in water. For example, on the top of the crests, the mean velocity is just equal to the velocity at the crest, and it does not mean that the velocity is equal on average to this value during the whole wave cycle. It would be more physical to compute the ensemble-average mean transport per wave cycle, $\overline{\boldsymbol{T}}_r(x,z)$, which is defined by:

$$\overline{\boldsymbol{T}}_r(x,z) = \frac{1}{n}\int_0^{nT} \delta(x,z,t)\boldsymbol{U}(x,z,t)\,\mathrm{d}t. \tag{5.2}$$

This quantity represents the average movement of a particle during a wave cycle. Figure 13 shows a map of the horizontal component of the non-dimensional transport $\overline{\boldsymbol{T}}_r/(T\sqrt{gD})$, with T the incipient wave period. It could be noted that under the trough envelope (e.g. points always located in the water), we have: $\overline{\boldsymbol{T}}_r(x,z) = T\ \overline{\boldsymbol{U}}(x,z)$,

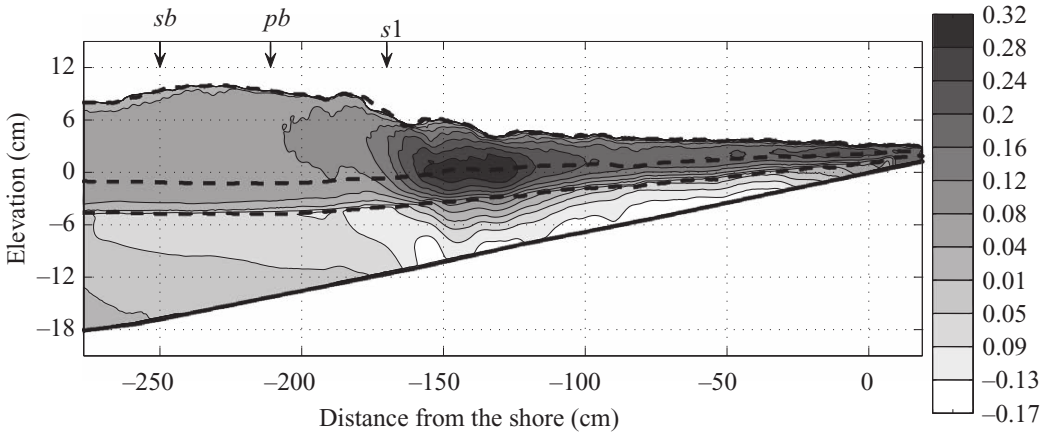

FIGURE 13. Map of the non-dimensional ensemble-time-averaged transport per wave cycle, $\overline{\boldsymbol{T}}_r(x, z)/(T\sqrt{gD(x)})$ (horizontal component).

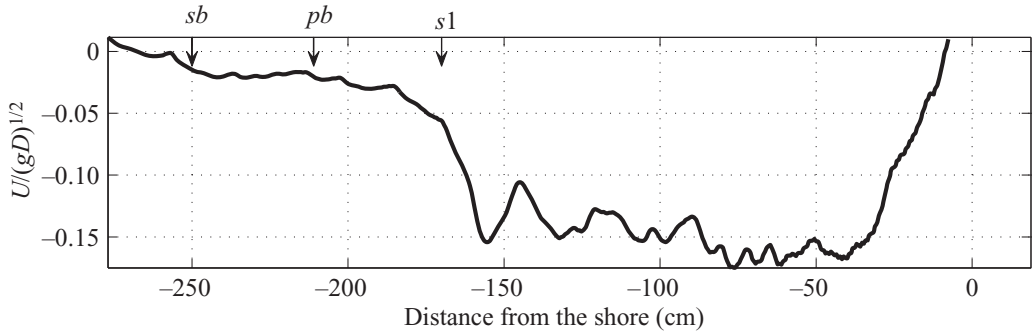

FIGURE 14. Cross-shore evolution of the non-dimensional mean horizontal velocity at the first PIV point above the beach.

so non-dimensional velocities and transport under the trough envelope line are equal: $\overline{\boldsymbol{T}}_r/(T\sqrt{gD}) = \overline{\boldsymbol{U}}(x, z)/\sqrt{gD}$. Figure 13 clearly shows that mean transport is shoreward above the trough-envelope and seaward under it. These results agree with data from Cox *et al.* (1995) and with LDV measurements by Stansby & Feng (2005). Maximum shoreward values are found during the splash-up events, and not during the plunging breaker event. The maximum seaward transport is situated near the bottom and extends from the splash-up location to the rolling phase. Figure 14 presents the cross-shore evolution of the non-dimensional average horizontal velocity very close to the bottom, at the first PIV grid point above the beach. Before breaking, horizontal velocity is approximately null. At the beginning of breaking, near-bottom-velocity increases and is directed offshore. Reverse flow reaches a maximum amplitude of $0.17\sqrt{gD}$ during the roller phase, then it decreases near the shoreline. We found positive velocity magnitudes close to the shoreline ($x > -9$ cm), but this is due to an underestimation of the offshore (e.g. negative) horizontal PIV measured velocities in this area. Near to the shore, the edge of the incoming breaker bore during the up-rush is relatively thick and the depth of the incoming wave is large enough to measure coherent velocities. But after breaking, when the flow is going back during the down-rush, the flow is shallow (see figure 15). The vertical water depth is approximately equal to one PIV cell interrogation window, and the PIV system is not accurate enough to measure velocities in such a region. More than two PIV cells in the vertical dimension (Adrian 1991) would be required for a better estimation of the velocities during the backrush event which follows the run-up. So our measured velocities

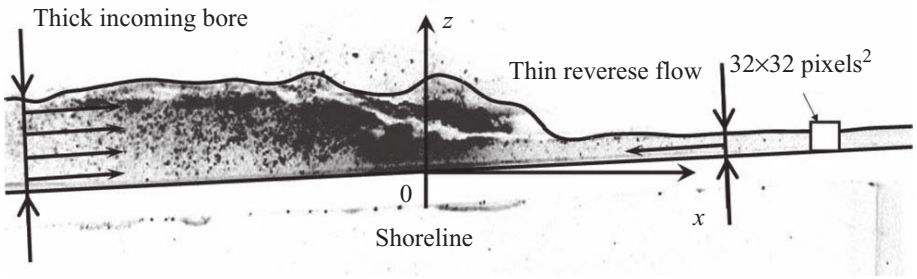

FIGURE 15. Explanation of the measured positive mean transport close to the shoreline.

during the back-rush are wrong in this area, and finally we have a positive bias for the computed mean velocity and transport near the shore. This uprush/downrush asymmetry, with a sudden large bore-advected turbulence during the uprush, and a long-time duration reverse flow with less turbulence during the downrush, has been previously observed by Cowen *et al.* (2003).

If we considered a two-dimensional flow, mass conservation should lead to a zero overall balance mean horizontal transport $\overline{\overline{T_r}}$:

$$\overline{\overline{T_r}} = \iint \overline{\boldsymbol{T}_r}(x, z) \cdot \boldsymbol{x} / (T \sqrt{g D(x)}) \, \mathrm{d}x \, \mathrm{d}z. \tag{5.3}$$

We actually found $\overline{\overline{Tr}} = 0.035$. There might be two reasons for this non-zero measured mean transport.

(i) As previously explained, for very shallow water measurement, e.g. near the shoreline, we underestimate negative velocities, so the overall budget is positive (see the positive cell at the right-hand side of figure 13). Considering only the part for $x \in [-280, -50]$ cm, mean mass transport decreases to a value $\overline{\overline{Tr}} = 0.031$.

(ii) Mainly above the mean sea level and during the breaking event, the flow is a turbulent aerated two-phase air–water flow, as analysed in Brocchini & Peregrine (2001*a*, *b*) For example, during the plunging event and the first splash-up, the impinging jet mixes with the water and a region of high concentration of air bubbles is developed. The bubble mass under the bore rises gradually while it translates horizontally. The bore front is always tumbling over and air bubbles carried by large eddies reach the bottom soon after the wavefront passes. A detailed investigation of mass transport must account for the influence of air-entraining flow. The density of the flow in a location surrounded by foam is lower than unity. The integral of the horizontal transport should be weighted by the density of the flow, $\rho(x, z)$:

$$\overline{\overline{T_{r\,corrected}}} = \iint \rho(x, z) \overline{\boldsymbol{T}_r}(x, z) \cdot \boldsymbol{x} / (T \sqrt{g D(x)}) \, \mathrm{d}x \, \mathrm{d}z. \tag{5.4}$$

This correction would lead to a lower value of $\overline{\overline{T_{r\,corrected}}}$ in comparison with $\overline{\overline{T_r}}$ because many positive velocities located near the crests should be weighed by lower density values, more particularly all along the splash-up regions. In the next section, we estimate the void fraction $\alpha(x, z)$:

$$\alpha(x, z) = 1 - \rho(x, z). \tag{5.5}$$

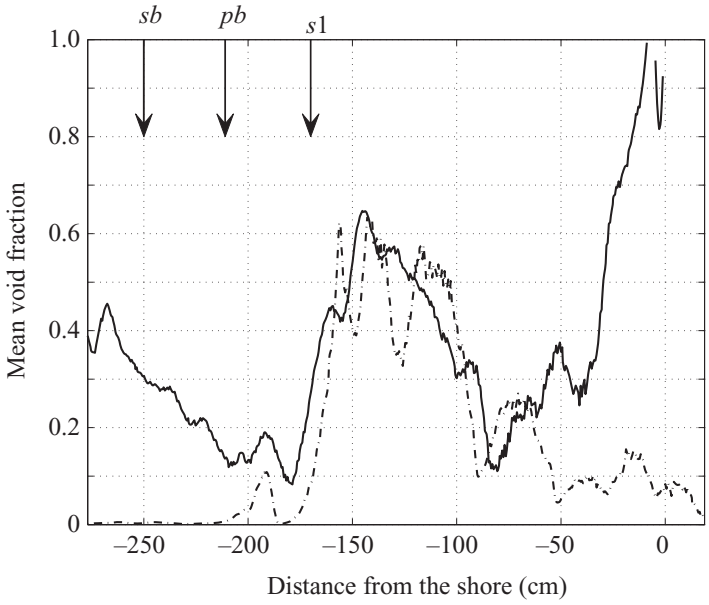

FIGURE 16. Void fraction: vertically integrated values $\alpha_{ZF}(x)$ and $\alpha_{LI}(x)$. —, zero flux method; · — ·, light intensity method.

6. Void fraction estimation

Studies of surf-zone air entrainment and void fraction estimation under breaking waves are limited because the flow fields of broken waves are complicated after mixing the air bubbles (Loewen & Melville 1994; Chanson, Aoki & Maruyama 2002). We estimated the void fraction with two different methods:

(i) *Zero-flux method* α_{ZF}

According to Govender *et al.* (2002), the vertically integrated void fraction can be estimated from the horizontal transport conservation. For each location x, the integral of the mean horizontal transport along the vertical water column should be equal to zero (this hypothesis is valid only if the ensemble average water flow is two-dimensional, which may not be true in the breaking region). It is possible to calculate the vertically averaged mean density $\rho_{ZF}(x)$ (and then the mean void fraction $\alpha_{ZF}(x)$) as the ratio between the reverse and the forward mean transport:

$$\left.\begin{aligned} \rho_{ZF}(x) &= \int_{z \text{ for } T_r(x,z)<0} \overline{\boldsymbol{T}}_r(x,z)\cdot\boldsymbol{x}\,\mathrm{d}z \Big/ \int_{z \text{ for } T_r(x,z)>0} \overline{\boldsymbol{T}}_r(x,z)\cdot\boldsymbol{x}\,\mathrm{d}z, \\ \alpha_{ZF}(x) &= 1-\rho_{ZF}(x). \end{aligned}\right\} \tag{6.1}$$

The vertical integrated mean void fraction, $\alpha_{ZF}(x)$, is presented in figure 16. Before breaking, $\alpha_{ZF}(x)$ is badly estimated because this parameter is here the ratio of two small values (onshore and offshore transport are close to zero). There is a local maximum value of $\alpha = 0.65$ during the splash-up event ($x \simeq -150$ cm). There is a strong air entrainment in this area. A small secondary maximum is found near $x = -50$ cm. Near the shoreline (for $x > -40$ cm), α values are incorrect because negative PIV velocities are badly estimated in that area. The shape of this curve, with two maxima, looks like the curve displayed in figure 6(*d*). Therefore, the observed differences between the wave gauge data and the water surface computed from PIV images seem to be related to the amount of aeration.

(ii) *Light–intensity method* α_{LI}

During the breaking process, on the raw PIV images, regions of mixed air–water flow are much brighter than regions without foam (see figure 4, windows $w6$ to $w14$). The

light intensity of each pixel of a PIV image, $I(x, z, t)$, is coded from 0 (black) to 255 (white). The brighter the light intensity, the larger the air entrainment. So we decided to estimate the void fraction from the light intensity of the images. The attenuation of the light intensity can be estimated using light-scattering theory (Mie theory). When the scatters are air bubbles, and the light comes from a monochromatic YAG laser (wavelength $\simeq$ 532 nm), the light scattering is described well by the laws of geometrical optics (Shamoun, EL Beshbeeshy & Bonazza 1999). When a light beam traverses a volume containing air bubbles, the ratio of incident to transmitted light intensity follows Lambert's law:

$$\frac{I(x, z, t) - I_0}{I_0} = -\exp(K\alpha_{LI}(x, z, t)), \tag{6.2}$$

with I_o a light-intensity constant and K an attenuation coefficient.

The constant I_o is matched to be the maximum of light intensity:

$$I_o = \max_{x,z} \overline{I}(x, z) \tag{6.3}$$

with:

$$\overline{I}(x, z) = \int_0^{nT} \delta(x, z, t) I(x, z, t)\, \mathrm{d}t \Big/ \int_0^{nT} \delta(x, z, t)\, \mathrm{d}t. \tag{6.4}$$

The attenuation coefficient K is obtained by matching the maximum of the vertically integrated ensemble-average void fraction computed with the two methods during the breaking event where air entrainment is important:

$$\max_{-250<x<-50}(\alpha_{ZF}(x)) = \max_{-250<x<-50}(\alpha_{LI}(x)), \tag{6.5}$$

with the vertically integrated ensemble-average void fraction defined by:

$$\alpha_{LI}(x) = \int_{-d(x)}^{\bar{\eta}_{Max}(x)} \alpha_{LI}(x, z)\, \mathrm{d}z \tag{6.6}$$

and the ensemble-average void fraction by:

$$\alpha_{LI}(x, z) = \int_0^{nT} \delta(x, z, t)\alpha_{LI}(x, z, t)\, \mathrm{d}t \Big/ \int_0^{nT} \delta(x, z, t)\, \mathrm{d}t. \tag{6.7}$$

By recursively matching (6.3) to (6.7), we finally obtained $K = 2.00$. Then the values of the void fraction in the whole domain were obtained from light-intensity images by inverting (6.2).

In order to validate this new void fraction determination technique from the raw PIV images, we have compared our results with the analytical solution of the diffusion equation for the void fraction distribution (Hoque & Aoki 2005). From Wu (1988) and Stanton & Thornon (2000) observations and Hoque & Aoki (2005) developments, the void fraction should consistently decay exponentially with depth under breaking waves:

$$\alpha_{LI}(x, z < 0) = \alpha_{LI}(x, z = 0) \exp(k_o z / H(x)) \tag{6.8}$$

with $k_o = 3.75$, the proportionality constant defined by Hoque & Aoki (2005) for the spilling case, and $H(x)$ the local wave height at abscissa x. Figure 17 compares the measured vertical profiles of the mean void fraction at different locations during the breaking event and the vertical profiles of the mean void fraction computed from (6.8). Clearly, we have good agreement between measured values and this semi-analytical formulation. The decay of the void fraction with depth is obviously

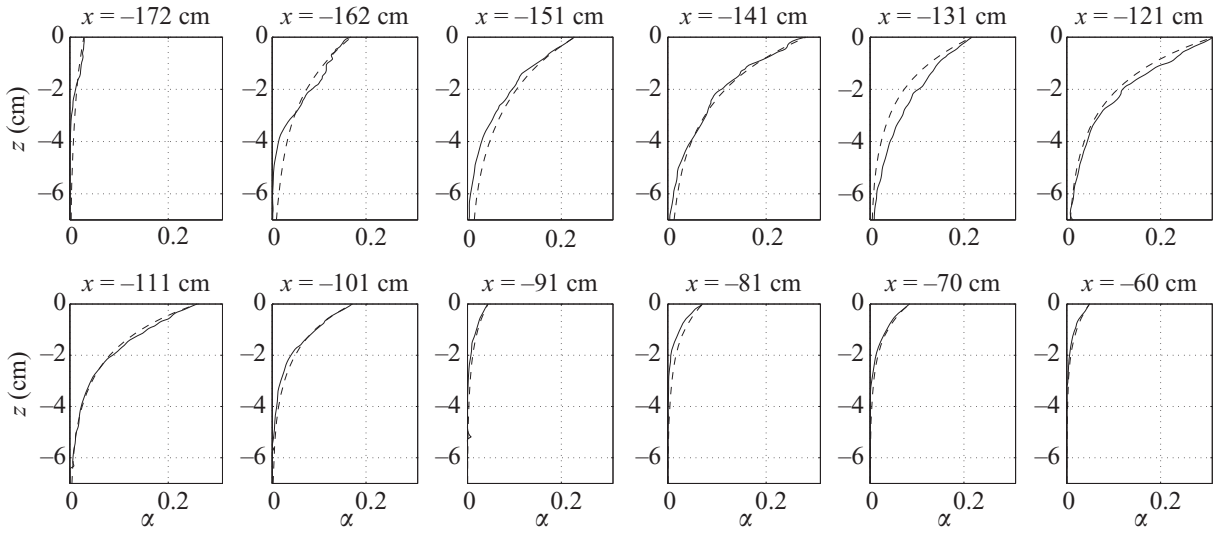

FIGURE 17. Measured vertical distribution of mean void fraction α_{LI} at different locations (solid line), and comparison with (6.8) (Hoque & Aoki 2005) (dashed line).

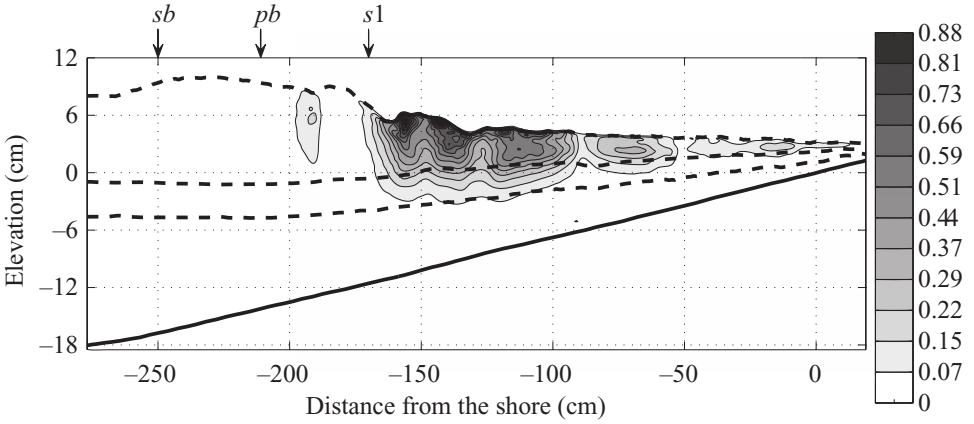

FIGURE 18. Map of the ensemble-averaged void fraction $\alpha_{LI}(x, z)$.

exponential and Hoque & Aoki (2005)'s formulation is a good approximation. At mean water level ($z = 0$), the void fraction is of the order of 0.25 during the splash-up event, then of the order of 0.1 during the spilling phase. At depth $z = -6$ cm, the void fraction is always close to zero. Hoque & Aoki (2005) obtained similar behaviour, but with slightly lower values of the void fraction at mean water level for spilling breakers on a 1/9.5 sloping bed.

Figure 18 gives a map of the ensemble-averaged void fraction $\alpha_{LI}(x, z)$. Void fraction values are close to zero everywhere under the trough envelope, and before the plunging event. We see clearly the air entrainment due to plunging, and then due to the successive splash-up sequences. Values of the void fraction are relatively high with a maximum value $\alpha_{max} = 0.88$ near the crest envelope, close to the first splash-up location. With an optical sensor that determines the refractive index on small area, Blenkinsopp & Chaplin (2005) measured void fraction values around $\alpha \simeq 0.8 - 0.9$ during the splash-up sequence of a waves breaking over an obstacle (see their figure 3). With a global conducting probe, Lamarre & Melville (1991, 1994) found also high void fraction plumes ($\alpha \simeq 0.5$) for waves breaking in deep water, close to the surface. After the splash-up, the void fraction decreases slowly above mean sea level during the bore-propagating phase, with values near 0.3, then near 0.2 close to the shore between the mean water level and the crest envelope. With a local conducting probe,

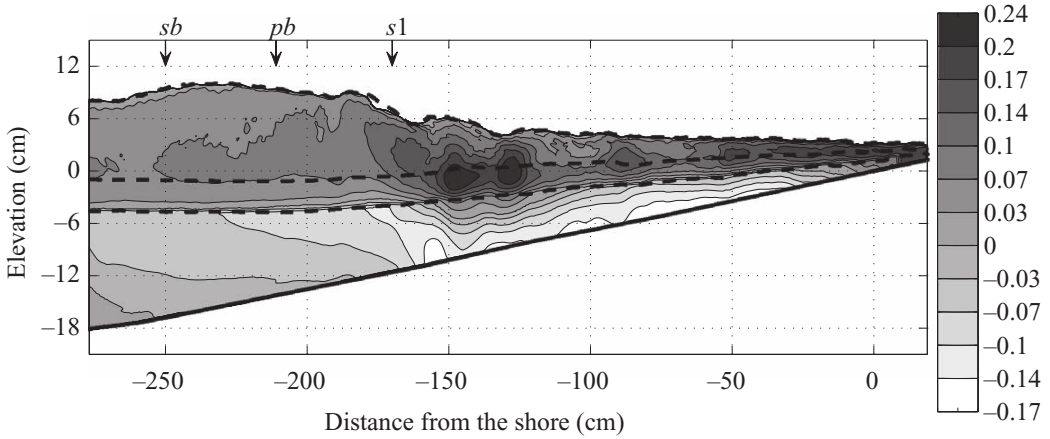

FIGURE 19. Map of ensemble-time-averaged transport per wave cycle corrected by the void fraction, $\overline{\boldsymbol{T}}_{r_{corrected}}(x, z)/(T\sqrt{gD(x)})$, (horizontal component).

Cox & Shin (2003) found relatively similar values of void fraction ($\alpha \simeq 0.2 - 0.3$) when the bore crossed the probe.

The vertically integrated void fraction by the light-intensity method was defined by:

$$\alpha_{LI}(x) = \int_{-d(x)}^{\bar{\eta}_{Max}(x)} \frac{\alpha_{LI}(x, z)}{\bar{\eta}_{Max}(x) + d(x)}\, \mathrm{d}z. \tag{6.9}$$

The comparison between the light-intensity method and the zero-flux method is presented in figure 16. For relatively deep water, the light-intensity method gives much better results with a void fraction close to zero. During the plunging phase, there is a first local small maximum found by the two methods at $x = -190$ cm. Then, the void fraction increases during the splash-up phase. There are some discrepancies between the two methods. The light-intensity method gives successive local maxima related to the successive splash-up sequences. After $x = -60$ cm, the two methods diverge with more coherent data from the light-intensity method.

The ensemble-averaged transport corrected by the void fraction, $\overline{\boldsymbol{T}}_{r_{corrected}}(x, z)$, defined by:

$$\overline{\boldsymbol{T}}_{r_{corrected}}(x, z) = (1 - \alpha_{LI}(x, z))\, \overline{\boldsymbol{T}}_r(x, z)/(T\sqrt{gD(x)}) \tag{6.10}$$

is shown in figure 19. Clearly, the amount of positive transport is reduced when the void fraction is taken into account. Maximum values of the transport occurred from the splash-up location to the shoreline between the mean sea level and the trough envelope. The overall integral of the corrected transport is now equal to $\overline{\overline{Tr}} = 0.020$ and if we consider only the part for $x \in [-280, -50]$ cm, the value decreases up to $\overline{\overline{Tr}} = 0.016$. This last value is 50 % lower than the value computed without void fraction correction (cf. § 5).

7. Phase average

We computed 3264 different instantaneous velocity fields representing 256 wave cycles. In order to have a statistical evolution of the periodic flow during a wave cycle, we computed a phase-average of velocities and water profiles by averaging all the instantaneous data that were acquired at the same phase. This procedure is commonly used to study periodic events. The incipient wave period was $T = 1.275$ s, and the PIV acquisition rate was 10 Hz. So the duration of 51 successive PIV velocity

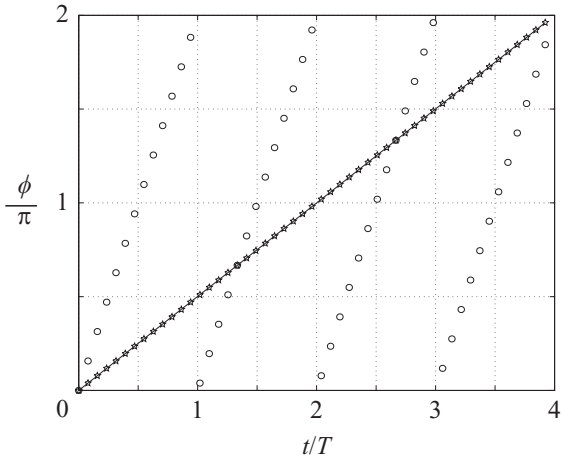

FIGURE 20. Time history of the phase distribution. ○, successive phases; ⋆, sorted phases.

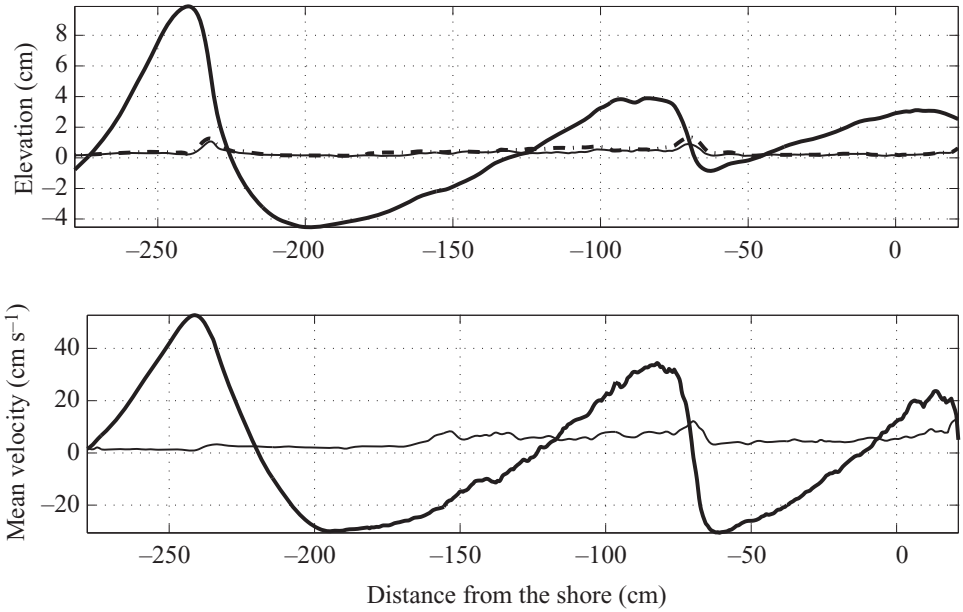

FIGURE 21. Example of phase-to-phase repeatability between the 64 different cycles for the phase $\varphi = 318°$: wave profile (up), depth integrated horizontal velocity (down). Bold line, phase average; thin line, standard deviation from spline surface reconstruction; dashed line, standard deviation from original raw surface data.

fields corresponded exactly to 4 wave periods: $51/10 = 4 \times T$. Consequently, all the PIV velocity fields separated by 51 PIV time steps were exactly in phase. As shown in figure 20, this technique allowed us to describe a wave period in 51 different phases. For each phase, the phase-average field is obtained by averaging the $256/4 = 64$ instantaneous fields corresponding to that phase.

The phase average was defined by:

$$\left.\begin{aligned} &\eta_{\varphi_i}(x) = \frac{1}{64}\sum_{j=1}^{64}\eta(x, t_{ij}),\ \boldsymbol{U}_{\varphi_i}(x, z) = \frac{1}{64}\sum_{j=1}^{64}\boldsymbol{U}(x, z, t_{ij}) \\ &\text{with} \\ &\qquad t_{ij} = (i + 4j \times 10T)\Delta t, \quad \varphi_i = \frac{2i\,\pi}{51} \\ &\qquad\qquad \text{for} \quad i \in [1, 51],\ \Delta t = 0.1\,\text{s} \end{aligned}\right\} \tag{7.1}$$

The phase-to-phase repeatability between the 64 different fields for a given phase is shown in figure 21: the mean profile and the standard deviation from the mean

profile are displayed for phase $\varphi = 318°$ for the water elevation and depth integrated horizontal velocity. For both the surface elevation and depth integrated horizontal velocity, the standard deviation is weak before breaking, even for the front of the wave ($x < -200$ cm). We observe small differences between the standard deviation computed from the raw surface contour data and the standard deviation computed from the surface spline interpolation. This result confirms the robustness of the reconstruction method. After breaking, a dispersion appears on the back face of the wave owing to the appearance of air–water mixing. The repeatability of the front face of the bore remains excellent. With Fourier analysis, we computed the phase of all the wave profiles. The phase-to-phase repeatability was statistically less than 1° (the standard deviation of all the phases that belonged to the same 'phase' was lower than 1°).

The water profile and the horizontal component of the non-dimensional phase-averaged velocity $\boldsymbol{U}(x, z)_\varphi / \sqrt{gD(x)}$ are presented in figure 22 for five different phases: $\varphi = 35°$, 106°, 176°, 247° and 318°. This is a new result, to present phase-average results in the space-domain (e.g. $U_\varphi(x, z)$) over the surf zone; previous published results have usually been presented in the time-domain (e.g. $U_\varphi(t)$ at each measurement point). We see clearly the wave height attenuation during the wave breaking, and the decreasing of the wavelength as the wave reaches the shoreline. Velocities are positive (shoreward) under the crests, in the whole water column, from the top of the crest to the bottom. Similarly, velocities are negative (seaward) under the troughs. Velocity maxima in non-dimensional form are around unity near the tops of the crests at the beginning of the plunging and reach 1.35 just after the splash-up phase. Negative velocities are around $-0.40\sqrt{gD}$ under the troughs. Before the plunging event, velocities are maximal on the same vertical line under the wave crest (see figure 22, phase $\varphi = 318°$, highest velocities in the water column are all located at abscissa $x = -240$ cm) but after this event, during all the wave breaking, there is a phase shift from the bottom to the crest, i.e. crest velocities are in advance of phase if they are compared with bottom velocities (see figure 22, phase $\varphi = 106°$, near the wave crest, velocity is a maximum at abscissa $x = -155$ cm and near the bottom velocity is maximum at abscissa $x = -175$ cm). This phase shift is due to (i) friction effects on the bottom which slow down velocities near the beach, and (ii) the negative transport near the bottom which acts against the wave. The shear of the current under the crests during the breaking process has been observed by Govender *et al.* (2002).

As explained in § 4, we used cubic smoothing spline interpolation to construct the velocity field over the whole surf zone. A major asset of the spline function is the direct use of calculated spline coefficients to compute space-derivatives $\partial/\partial x$ and $\partial/\partial z$, without noise contamination (Spedding & Rignot 1993; Fouras & Soria 1999; Cohn & Koochesfahani 2000). With this technique, we avoid the use of the first-order difference scheme, therefore the quantities calculated with derivatives are calculated with the same spatial discretization $\mathrm{d}x = \mathrm{d}z = 0.592$ cm.

Chang & Liu (1998, 1999) found that the vorticity generated by wave breaking, under the trough envelope, was of the same order of magnitude as phase speed divided by local depth: $\Omega(x) \simeq (\sqrt{gD(x)}/D(x))$. Therefore, we calculated the dimensionless phase-averaged vorticity field $\Omega_\varphi(x, z) = \|\nabla \otimes \boldsymbol{U}_\varphi(x, z)\| / \sqrt{g/D(x)}$. The results are shown in figure 23 for the same phases as figure 22. A large clockwise vortex structure appears first on the front side of the wave crest at the beginning of the plunging phase (phase $\varphi = 35°$). This vortex is not localized at the top of the crest, but rather at the toe of the front, just above the mean sea level. Peregrine & Svendsen (1978) were the first to observe that vorticity was generated at the toe of the incipient breaking crest. The vorticity magnitude increases during the plunging. The first splash-up sequence

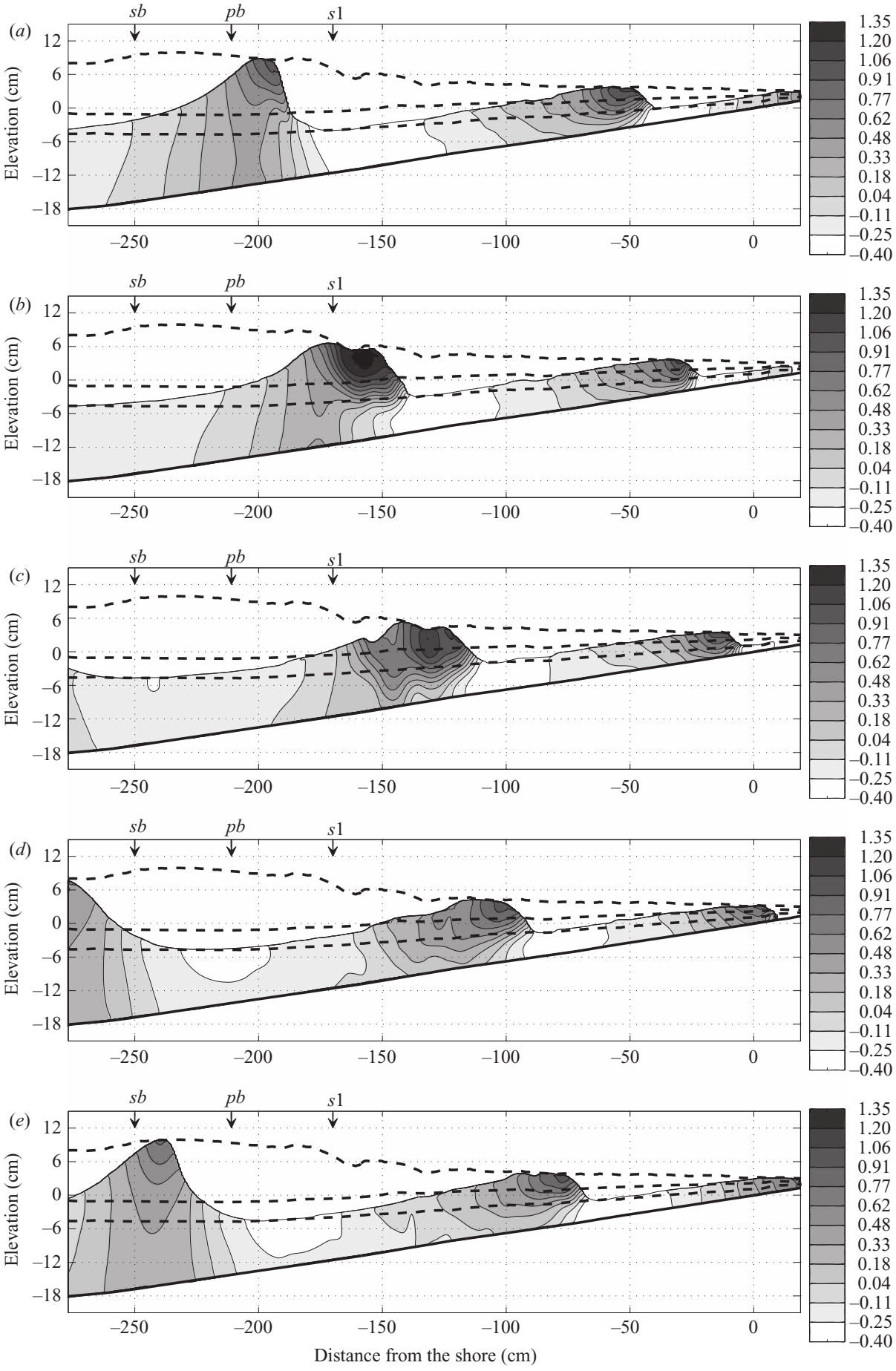

FIGURE 22. Horizontal component of non-dimensioned phase-averaged velocities $U_\varphi(x, z)/\sqrt{g\,D}$; (*a*) $\varphi = 35°$, (*b*) 106°, (*c*) 176°, (*d*) 247° and (*e*) 318°.

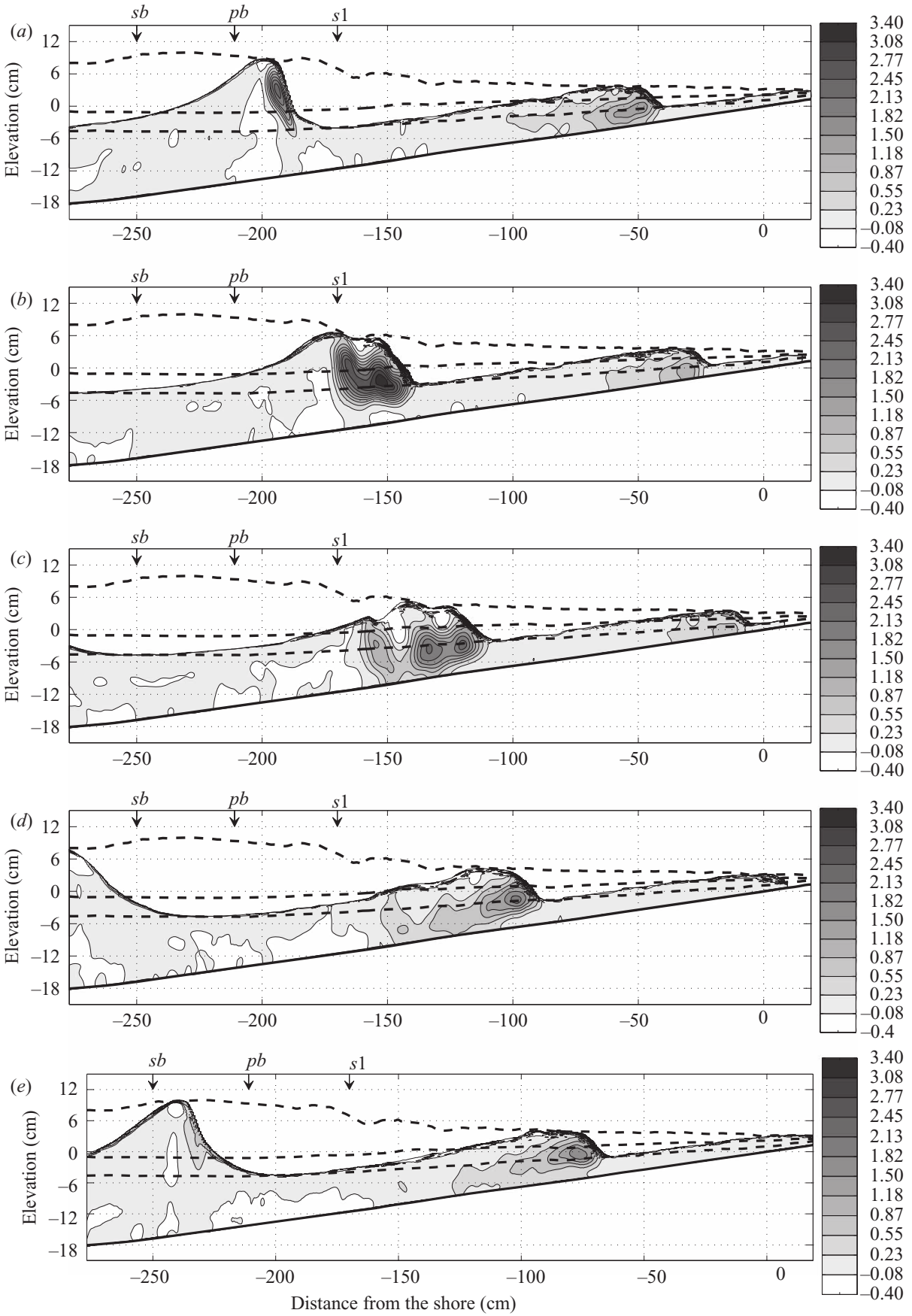

FIGURE 23. Non-dimensioned phase average vorticity $\Omega_\varphi(x, z)/\sqrt{g/D(x)}$; (*a*) $\varphi = 35°$, (*b*) 106°, (*c*) 176°, (*d*) 247° and (*e*) 318°.

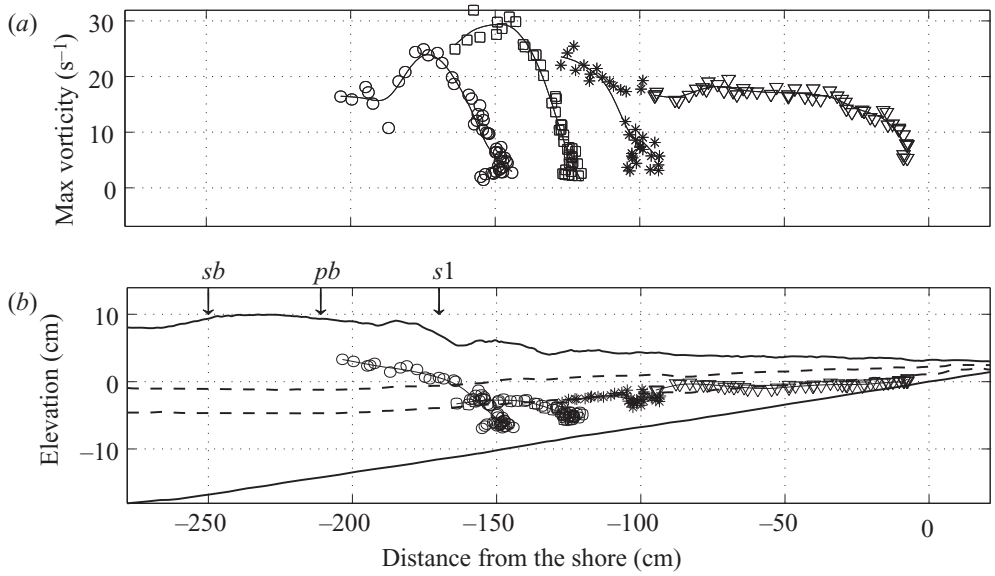

FIGURE 24. (*a*) Intensity and (*b*) Position of the four observed vortices generated during a wave cycle: ○, first; □, second; ∗, third; △, fourth.

creates a new vortex ahead of the first one (see $\varphi = 106°$). Then successive vortices are generated during the following splash-up sequences ($\varphi = 176°$) and ($\varphi = 318°$). These vortices are the 'horizontal eddies' described by Nadaoka *et al.* (1989) in their schematic representation of large-scale eddies under breaking waves, and also illustrated by Christensen, Walstra & Emerat (2002) in their figure 4. They called them 'horizontal' because their main axis is horizontal. The formation of vortices during a splash-up event is illustrated by Lubin *et al.* (2006) in their large-eddy simulation numerical study of breaking waves (see their figures 12 to 15). In non-dimensional form, clearly the vorticity magnitude is of the order of $\sqrt{gD(x)}/D(x)$, more particularly during the bore propagating phase at low depth.

The intensity and location of the vortices generated during a wave cycle are presented in figure 24. The first vortex moves on shore with increasing magnitude during the plunging phase, then propagates more slowly downward with a decreasing intensity at the beginning of the first splash-up sequence. The second vortex, initiated by the first splash-up, reaches $30\,\mathrm{s}^{-1}$, moves shoreward and then downward with a decreasing magnitude. The third and fourth vortices move towards the shoreline along the trough-envelope line. Their magnitude is of the order of $20\,\mathrm{s}^{-1}$ when they propagate near the bore-front, then they slow-down and vanish slowly when they go deeper, dissipated by bottom friction and slowed down by mean return flow.

With LDV, for similar depth but for a higher experimental self-similarity parameter, Stansby & Feng (2005) measured higher vorticity values during the plunging phase ($\Omega_{max} = 65\,\mathrm{s}^{-1}$), with also a concentrated vorticity ($\Omega = 35\,\mathrm{s}^{-1}$) in the roller region, moving with the bore front. Their measured vorticity magnitude decreases slightly as the bore moves towards the shore. The difference in magnitude could be due to the higher surf similarity parameter with a more pronounced plunging, or it could be that the higher spatial resolution possible using LDA (obtained by moving the probe position in the z-direction) enables the local peak value to be determined more accurately. In our experiment, we measured vorticity lower than those for hydraulic jumps of similar Froude number, whereas in Stansby & Feng (2005) the value at the beginning of breaking was similar to hydraulic jumps; but their values were below inshore.

The phase-average void fraction $\alpha_\varphi(x,z)$ was computed from the void fraction data $\alpha_{LI}(x,z,t)$ measured with the light-intensity method. We used a formulation similar to (7.1):

$$\alpha_{\varphi_i}(x,z) = \frac{1}{64}\sum_{j=1}^{64}\alpha_{LI}(x,z,t_{ij}), \tag{7.2}$$

with

$$t_{ij} = (i+4j\times 10T)\Delta t, \quad \varphi_i = \frac{2i\,\pi}{51} \quad \text{for} \quad i\in[1,51],\ \Delta t = 0.1\text{s}$$

Space–time evolution of the phase-average void fraction is shown in figure 25, for the phases presented in figures 22 and 23. We used the logarithmic intensity void fraction scale presented by Blenkinsopp & Chaplin (2005) which allows a better localization of the highly aerated areas. During the plunging phase, aeration is located inside the overturning lip (phase $\varphi = 35°$). During the splash-up sequence, the aeration is localized between the two vortices (phase $\varphi = 106°$). Then, during the bore-propagating phase, the maximum void fraction is not localized exactly at the edge of the bore front, but more behind the front-face of the wave (phase $\varphi = 176°$ and $\varphi = 247°$). Close to the shore, aeration is still present at the front face of the wave, but also at the back face of the wave near the crest ($\varphi = 318°$).

8. Fluctuating components around phase-average

For each of the 51 wave phase φ_i, we have 64 different velocity fields $\boldsymbol{U}(x,z,t_{ij})$, $j\in[1,64]$, $i\in[1,51]$. To go further than standard phase-averaged computations, we analysed velocity fluctuations around their own phase-averaged values. Using Reynolds-type decomposition, for an instantaneous full field measurement $\boldsymbol{U}(x,z,t_{ij})$, we wrote:

$$\boldsymbol{U}(x,z,t_{ij}) \;=\; \boldsymbol{U}_{\varphi_i}(x,z) \;+\; \boldsymbol{U}'(x,z,t_{ij}) \tag{8.1}$$

with

$$\boldsymbol{U}'(x,z,t_{ij}) = u'(x,z,t_{ij})\,\boldsymbol{x} + v'(x,z,t_{ij})\,\boldsymbol{y} + w'(x,z,t_{ij})\,\boldsymbol{z}$$

$\boldsymbol{U}'(x,z,t_{ij})$ is the difference between instantaneous velocity field $\boldsymbol{U}(x,z,t_{ij})$ and the corresponding phase averaged value $\boldsymbol{U}_{\varphi_i}(x,z)$ (see (7.1)). $\boldsymbol{U}'(x,z,t_{ij})$ could be considered as a deviation, or a fluctuation, around the mean value $\boldsymbol{U}_{\varphi_i}(x,z)$ (e.g. Cox *et al.* 1995; Ting & Kirby 1995, 1996; Cox & Anderson 2001)).

A quantity that characterizes physical transfers of energy is the so-called 'fluctuating kinetic energy per unit mass' at phase φ_i, $\overline{q'^2_{\varphi_i}}(x,z)$, defined by:

$$\overline{q'^2_{\varphi_i}}(x,z) = \tfrac{1}{2}\left(\overline{u'^2_{\varphi_i}}(x,z) + \overline{v'^2_{\varphi_i}}(x,z) + \overline{w'^2_{\varphi_i}}(x,z)\right), \tag{8.2}$$

with $\overline{u'^2_{\varphi_i}}$, (respectively, $\overline{v'^2_{\varphi_i}}$ and $\overline{w'^2_{\varphi_i}}$), the mean square value of the horizontal cross-shore (respectively, horizontal alongshore and vertical upwards) component of fluctuating velocities $\boldsymbol{U}'(x,z,t_{ij})$:

$$\overline{u'^2_{\varphi_i}}(x,z) = \frac{1}{64}\sum_{j=1}^{64}u'^2(x,z,t_{ij}). \tag{8.3}$$

To simplify the notation, subscript i is now removed: φ stands for φ_i. Since our PIV measurements provide only two components of the flow $\boldsymbol{U}$ (cross-shore u and vertical w components), but not the horizontal transverse component v, fluctuating

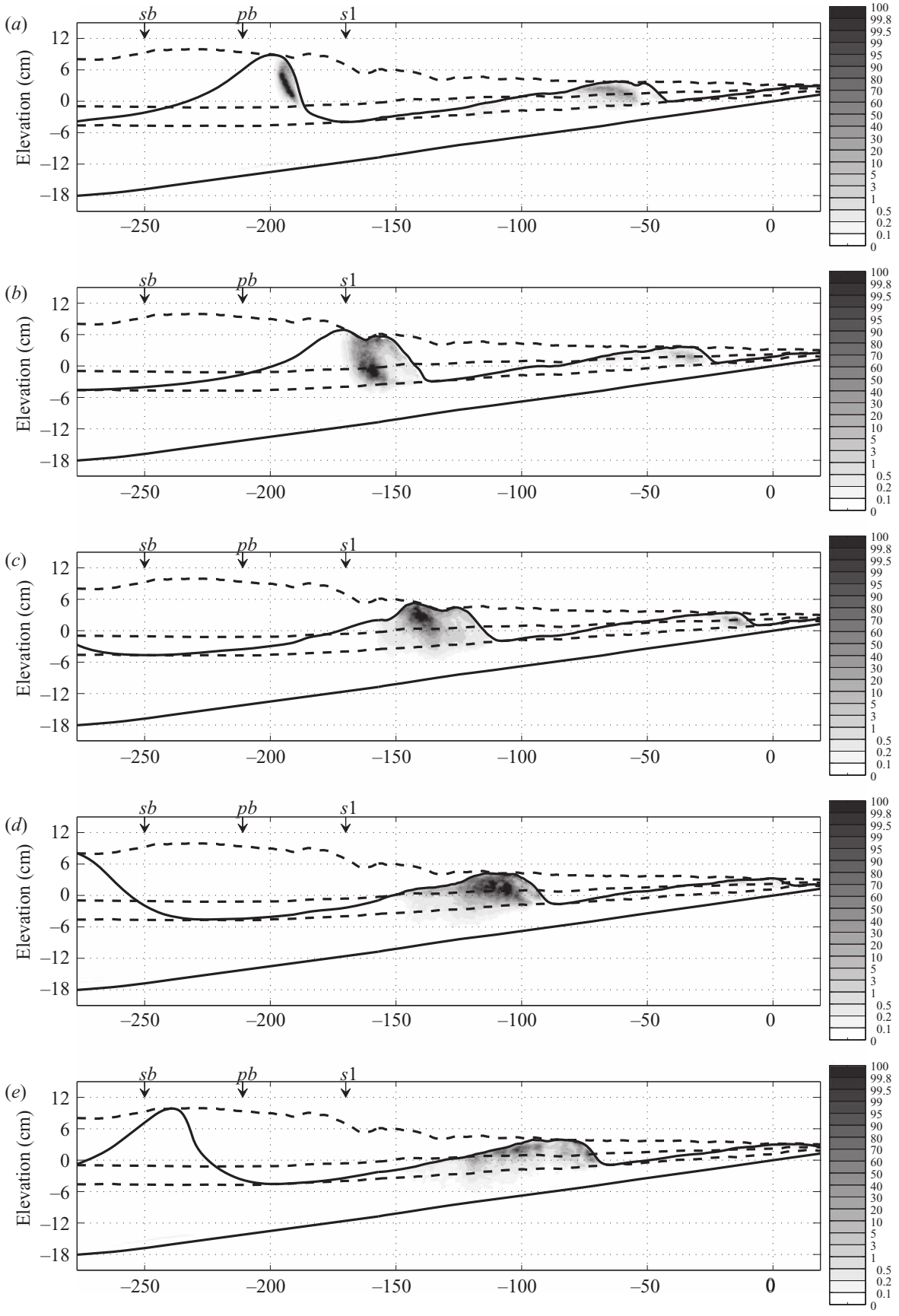

FIGURE 25. Phase average void fraction; (*a*) $\varphi = 35^\circ$, (*b*) 106°, (*c*) 176°, (*d*) 247° and (*e*) 318°.

kinetic energy $\overline{q_\varphi'^2}$ is estimated using the standard approximation for surf zone flow (Svendsen 1987):

$$\overline{q_\varphi'^2} = \frac{4}{3}\frac{\left(\overline{u_\varphi'^2} + \overline{w_\varphi'^2}\right)}{2} \tag{8.4}$$

which means that $\overline{v_\varphi'^2}$ is approximated by:

$$\overline{v_\varphi'^2} = \tfrac{1}{3}\left(\overline{u_\varphi'^2} + \overline{w_\varphi'^2}\right). \tag{8.5}$$

A commonly used physical fluctuating velocity scale is $\sqrt{\overline{q_\varphi'^2}}$. Evolution of $\sqrt{\overline{q_\varphi'^2}}$ with space and wave phase is important for the study of breaking-wave effects on flow dynamics and the environment. For example, the probability of sediment movement is related not only to the intensity of the mean flow, but also to the kinetic fluctuating intensity near the bottom boundary layer (Dancey & Diplas 2003). Space–time evolution of this velocity scale is shown in figure 26, in terms of Froude-scaled phase-averaged turbulent kinetic energy: $\sqrt{\overline{q_\varphi'^2}}/\sqrt{gD}$, with D the local mean water depth ($D = \bar{\eta} + d$), for the phases presented in figures 22 and 23. This figure identifies clearly the top of the front side of the breaking crest as the initiation point for fluctuation generation ($\varphi = 318°$). Values of $\sqrt{\overline{q_\varphi'^2}}$ increase during the plunging event ($\varphi = 35°$), and the splash-up phase ($\varphi = 106°$). Then, generated fluctuations are spread downstream and towards the bottom ($\varphi = 176°$). At this phase, we found again three cells of fluctuating intensities, but their location differs slightly from the location of the three vorticity cells found in figure 26 at phase $\varphi = 176°$. The centres of the $\sqrt{\overline{q_\varphi'^2}}$ cells are located on the edge of the vorticity cells, just above, or under them. At this phase, a local maximum is found near the bottom. During the rolling phase, after the splash-up, the non-dimensional velocity scale attached to the bore does not seem to decrease until the bore reaches the shoreline. The fluctuating intensity is maintained by the moving breaking process. Fluctuating intensity declines after the passage of the bore. Values are nearly zero under the trough on the back-side of the incipient dominant wave, and around 0.05 under the trough of the wave just behind the propagating bore.

Amplitudes of fluctuating energy can be compared with results of Mocke (2001) (see their figure 1 for comparison with many other data sets): their Froude-scaled turbulent kinetic velocity scale is in the range 0.03–0.07, but their data concern only measurements under the mean sea level $\bar{\eta}(x)$. Ting & Kirby (1995) found a maximum value of 0.1 just below the trough level. We found similar values under the trough line, except during and after the slash-up event with values up to 0.3 near the bottom. Maximum intensities were found, however, in the front part of the crests, above the trough line during the splash-up events ($\max \sqrt{\overline{q_\varphi'^2}}/gD \simeq 0.4$). Ting & Kirby (1995) found also maximum values of $\overline{q'^2}$ just after the first jet-splash cycle. To compare our results with previous published experiments, we have plotted (figure 27) the vertical profile of the square root ensemble time-averaged non-dimensional fluctuating energy. The ensemble time-averaged fluctuating energy is defined by:

$$\overline{\overline{q'^2}}(x, z) = \frac{1}{nT}\int_0^{nT} \delta(x, z, t)\overline{q'^2}(x, z, t)\,\mathrm{d}t. \tag{8.6}$$

The vertical profile is plotted at $x = -100$ cm, at the end of the splash-up region and at the beginning of the propagating bore region. It is compared with Ting & Kirby (1994) results and Govender *et al.* (2002) results (we use the $\overline{u'}$ and $\overline{w'}$ data plotted in

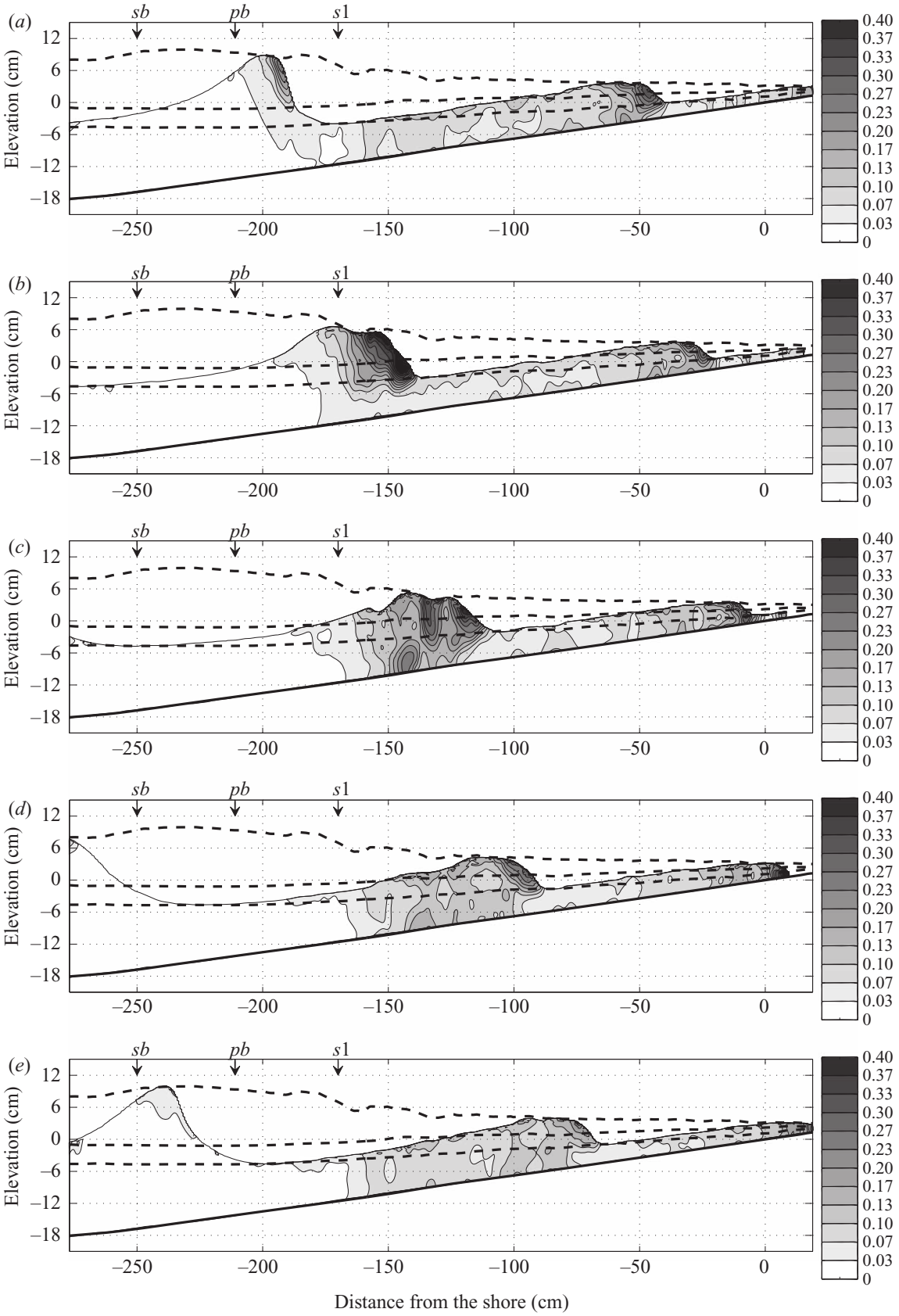

FIGURE 26. Phase-locked Froude normalized fluctuating kinetic energy $(\overline{q_\varphi'^2}/gD)^{1/2}$; (*a*) $\varphi = 35°$, (*b*) 106°, (*c*) 176°, (*d*) 247° and (*e*) 318°.

their figure 24-middle at station 3 for test 2, with their formula: $q'^2 = 1.33\,(u'^2 + w'^2)/2)$. Profiles are similar, with increasing values of $\sqrt{\overline{q'^2}}$ from the bottom to the trough envelope line $(0 < (z + d)/d < 0.6)$, and decreasing values from the trough envelope

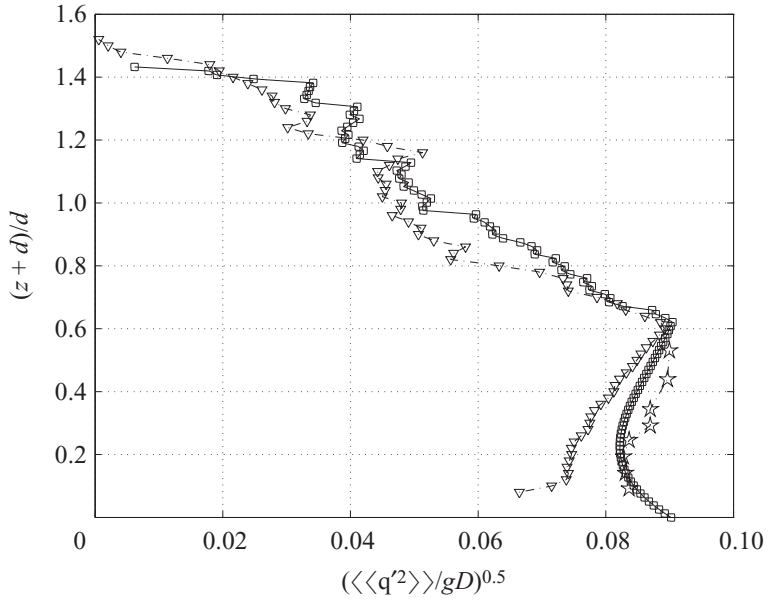

FIGURE 27. Vertical profile of non-dimensional ensemble time-average fluctuating kinetic energy scale $\sqrt{\overline{\overline{q'^2}}/gD}$. ☆, Ting & Kirby 1994; Govender *et al.* 2002; △, our PIV measurements at location $x = -100\,\mathrm{cm}$ □.

to the top of the crest ($0.6 < (z+d)/d < 1.5$). Our values are close to Ting & Kirby (1994) values under the trough line and to Govender *et al.* (2002) values above it. We found, moreover, a negative gradient of q'^2 close to the bed.

An important aspect would be the effect of the smoothing parameter, p, in the calculation of all the results. To illustrate this influence, some examples with $p = 0.99$ (i.e. almost no smoothing) are given (figure 28) for the horizontal velocity, vorticity and fluctuating kinetic energy scale. They must be compared with the results presented in figures 22, 23 and 26 for phase $\varphi = 176°$, which were calculated with a smoothing parameter $p = 0.5$. For the velocity and vorticity fields, the discrepancies are very weak. For the fluctuating kinetic energy scale, there are some local variations near the maxima, but nevertheless, looking at the two graphs, the discrepancies are not large. The root mean square difference between the two fields $\sqrt{\overline{q'^2}_{\varphi,p=0.50}/gD}$ and $\sqrt{\overline{q'^2}_{\varphi,p=0.99}/gD}$ was found to be 0.015. This value represents 4 % of the maximum of ($\sqrt{\overline{q'^2}_{\varphi,p=0.99}/gD}$) value, and 18 % of the mean of ($\sqrt{\overline{q'^2}_{\varphi,p=0.99}/gD}$).

In order to illustrate the influence of window gathering and smoothing, we calculated also the phase-average of the fluctuating kinetic energy for each of the 14 elementary windows, directly from the elementary PIV velocity fields of the 14 windows. The fourteen $\sqrt{\overline{q'^2_\varphi}}$ fields are gathered in figure 28(d) without any interpolation, and should be compared with figure 28(c). Boundaries between the windows are visible, but there are no large discrepancies between the two plots. Consequently, despite some local errors, the effect of the interpolation and smoothing of the velocity field on the fluctuating quantities does not seem large. The interpolation/smoothing procedure allows us to present global $\sqrt{\overline{q'^2_\varphi}}$ fields with no discontinuities.

Bottom shear stress plays a major role in the surf zone physical processes, for example in sediment transportation and turbulent kinetic energy balance near the bed (Cox & Kobayashi 1997; Trowbridge & Elgar 2001). Figure 29(a) represents the

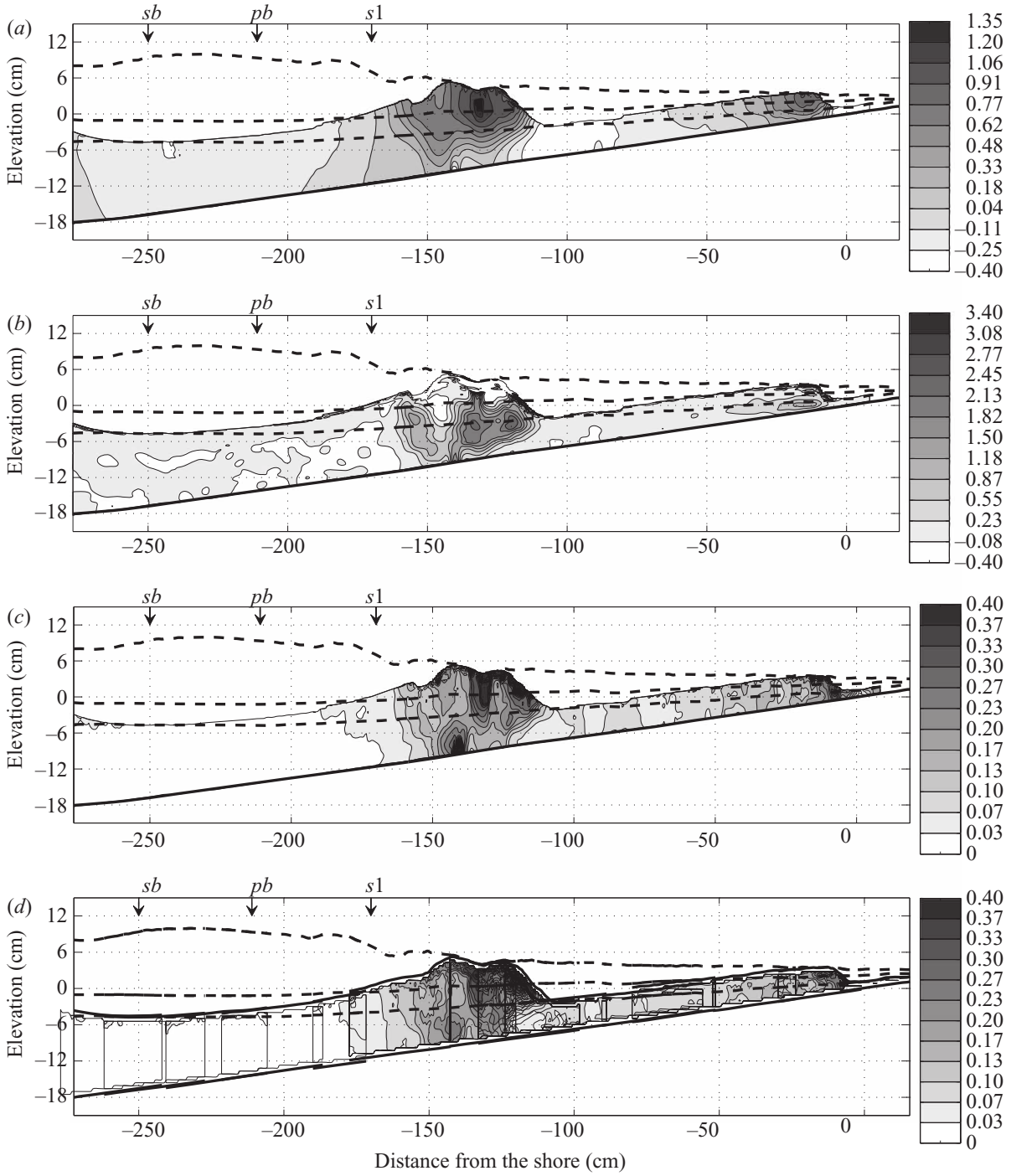

FIGURE 28. For $\varphi = 176°$, same as figures 21, 22 and 25, but with a smoothing value of 0.99 (i.e. almost no smoothing); (*a*) Non-dimensional horizontal velocity $U_{\varphi,p=0.99}/\sqrt{gD}$, (*b*) non-dimensional vorticity $\Omega_{\varphi,p=0.99}/\sqrt{g/D}$, (*c*) Froude normalized fluctuating kinetic energy scale $\sqrt{\overline{q'^2}_{\varphi,p=0.99}}$, and (*d*) Froude normalized fluctuating kinetic energy scale calculated for each of the 14 elementary windows directly from the elementary PIV fields without interpolation and smoothing.

ensemble-averaged Reynolds shear stress, $(\overline{U(x,z)W(x,z)})$, under the trough level. Values above the trough envelope are not presented, because they are about ten times higher than values under the troughs, and we preferred to use an appropriate zoom-scale under the troughs in order to see better the stress variations near the sloping beach. The stress is mainly negative in the splash-up and rolling regions, which means

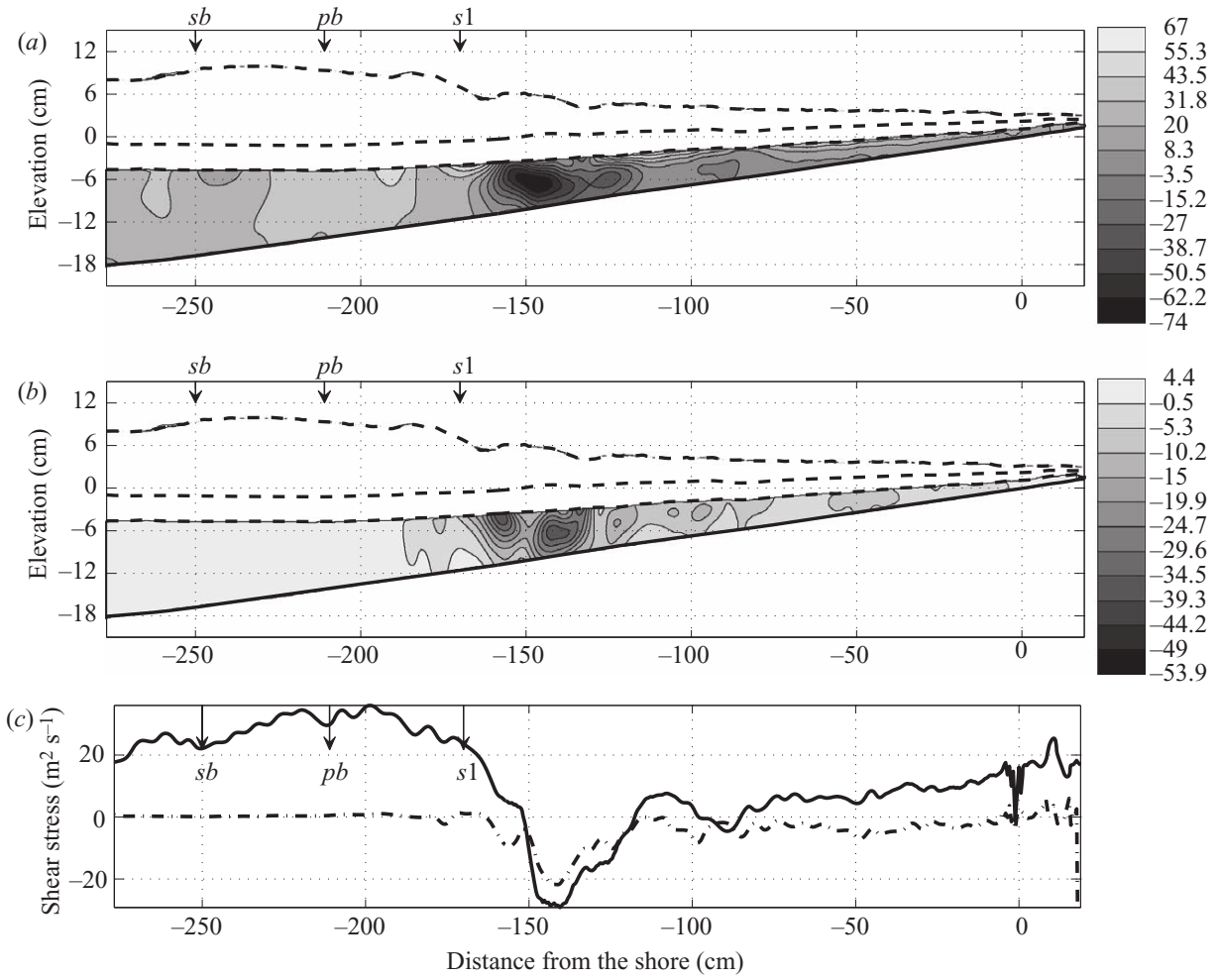

FIGURE 29. Ensemble average shear stress. (*a*) Reynolds shear stress under trough level ($\overline{UW}$), (*b*) fluctuating shear stress under trough level ($\overline{u'w'}$), (*c*) bottom shear stress at the first PIV point above the beach (solid line, ($\overline{UW}$); dashed line, ($\overline{u'w'}$)). Units in $\mathrm{cm}^2\,\mathrm{s}^{-2}$.

that transfers occur mainly onshore/downward or offshore/upward in that area. On the contrary, the mean stress is slightly positive before breaking and during the plunging phase. There is a well-localized minimum just after the start of the splash-up near $x = -150\,\mathrm{cm}$ when the lip of the splash-up hits the water. De Serio & Mossa (2006) found slightly lower values (stress around $-30\,\mathrm{cm}^2\,\mathrm{s}^{-2}$) for their plunging/spilling test 1. The ensemble-average fluctuating shear stress ($\overline{u'(x,z)w'(x,z)}$) is shown in figure 29(*b*). Again, values above the trough line are not presented because they are ten times higher. Values are negative almost everywhere which means that near the bed, fluctuations would induce sediment transportation onshore/downward or offshore/upwards. However, values are very weak before plunging. There are two distinct negative cells apart from $x = -150\,\mathrm{cm}$, related to the existence of the distinct vorticity cells that appear during the splash-up phase. Misra *et al.* (2005) measured also cells of shear stress under quasi-static spilling breakers. The bed shear stress very close to the bottom (at the first PIV point above the bed) is shown in figure 29(*c*). Reynolds-averaged and fluctuating components of the stress are both plotted. Near the bed, Reynolds stress is always positive, except near the splash-up region, which means that transfers very close to the bottom would be directed offshore except during the strong splash-up event. In this location, fluctuating stress is negative, whereas it is almost zero everywhere else. Stansby & Feng (2005) found fluctuating stress values of the order of $-25\,\mathrm{cm}^2\,\mathrm{s}^{-2}$ near the bed, which is close to our measured values.

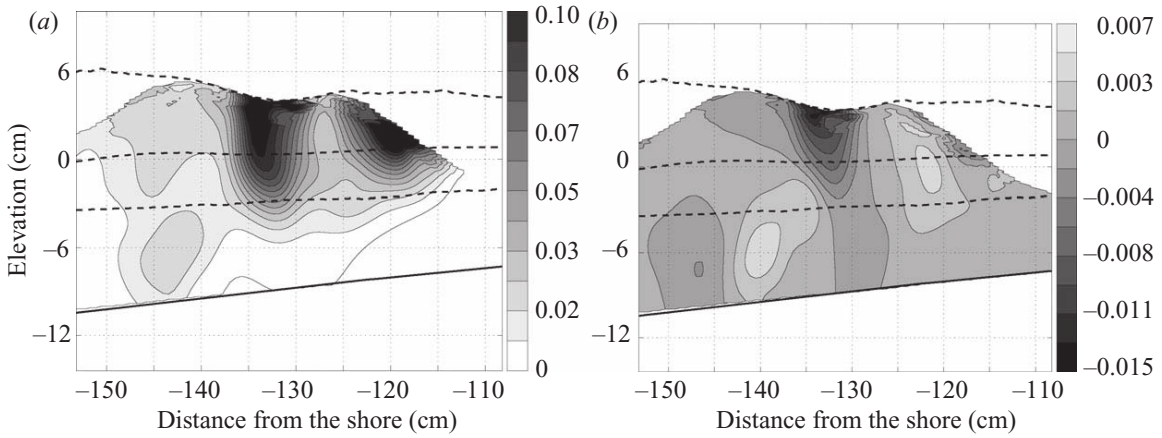

FIGURE 30. Example of non-dimensional phase-locked fluctuating energy transports by mean flow: phase $\varphi = 176°$, (*a*) $(U\,\overline{q'^2})_\varphi/(gD)^{3/2}$; $(W\,\overline{q'^2})_\varphi/(gD)^{3/2}$.

An example of the horizontal and vertical fluctuating energy transports by the mean flow are shown in figure 30 for the phase $\varphi = 176°$. High values of the transport terms are located mainly under the breaking wave, so we restricted the view to the crest, i.e. from $-155\,\text{cm} < x < -105\,\text{cm}$, during the splash-up sequence. Clearly, fluctuating kinetic energy is mainly transported by the rolling wave crest towards the shore. High values of the transport are all localized above the trough line. There are two convection cells, related to the successive eddies that appear at this phase (see figure 23, phase $\varphi = 176°$). The vertical transport is one order of magnitude lower than the horizontal one. Looking from the right to the left, the vertical transport is slightly downward at the air/water interface in the front part of the wave, then upward under the splash-up crest, then strongly downward between the two local wave maxima, and finally slightly upward on the opposite face. De Serio & Mossa (2006) found that the energy flux under the crest could be upward for spilling breakers, and we found similar values (around $0.002\,\text{m}^3\,\text{s}^{-3}$) in dimensional form at $z = -3\,\text{cm}$ under the mean sea level. We obtained much greater values than those of Ting & Kirby (1996), but their measurements were restricted under the trough line. Under the trough line, we found effectively much lower values than those measured near the crests. There are also two other transport cells which are located near the bottom: the upward one is located on the left-hand side of the main vortex at $x = -140\,\text{cm}$ (velocity is upward on the left of a positive vortex), and the downward one is located on the right-hand side of the third small vortex at $x = -146\,\text{cm}$ (velocity is downward on the right of a positive vortex).

Similarly, transport by fluctuations $(u'\,\overline{q'^2})_\varphi/(gD)^{3/2}$ and $(w'\,\overline{q'^2})_\varphi/(gD)^{3/2}$ were calculated. We do not present these terms here; they are mainly concentrated in the rolling phase near the front part of the crest, and its maximum seems to be attached to the front face of the roller.

Evolution of fluctuating kinetic energy can be modelled by the kinetic energy balance equation (Hinze 1975) which relates the total derivative $\text{D}\,\overline{q'^2}/\text{D}t$ with (i) transport terms due to convection, pressure gradients, and fluctuations, (ii) kinetic energy production terms and (iii) dissipation and diffusion terms. In the Appendix, we have developed the expression of all these terms using's Svendsen's (1987) approximation that relates non-measured alongshore velocity variations with measured cross-shore and vertical variations. Except for pressure terms that were beyond the capability of our experimental apparatus, these terms are a combination of

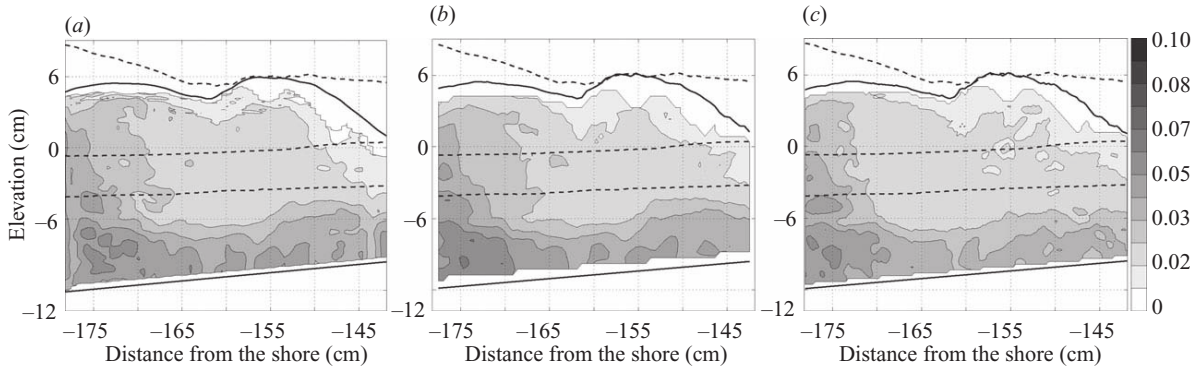

FIGURE 31. Kolmogorov length scale $(\nu^3/\varepsilon)^{1/4}$ (in cm) for phase $\varphi = 113°$; (*a*) zoom from the full field gathering/smoothing ($p = 0.99$) reconstruction; (*b*) computed from window number w6 and spatial resolution $\mathrm{d}x = \mathrm{d}z = 0.592$ cm with 32×32 pixels elementary PIV interrogation boxes; (*c*) computed from window number w6 and spatial resolution $\mathrm{d}x = \mathrm{d}z = 0.296$ cm with $16 \times 16_{\mathrm{pixels}}$ elementary PIV interrogation boxes.

space-derivatives, $\partial/\partial x$ and $\partial/\partial z$ of several tensor products with variables that we were able to measure (e.g. phase-averaged velocity $\boldsymbol{U}_\varphi$ and associated fluctuating component $\boldsymbol{U}'$, equation (8.1)). As explained in § 4, a major asset of the spline interpolation technique is the direct use of calculated spline coefficients to compute space-derivatives $\partial/\partial x$ and $\partial/\partial z$, without noise contamination (Cohn & Koochesfahani 2000). Therefore the quantities calculated with derivatives are calculated with the same order of spatial discretization ($\mathrm{d}x = \mathrm{d}z = 0.592$ cm). However, to measure the different terms of the kinetic balance equation, the spatial resolution must be of the order of ten times the Kolmogorov length scale (Cowen & Monismith 1997). The Kolmogorov length scale could be defined by

$$\eta_k = \left(\frac{\nu^3}{\varepsilon}\right)^{1/4}, \tag{8.7}$$

where ν is the kinematic viscosity, and ε the isotropic dissipation rate in the homogeneous turbulence. The dissipation rate ε is given in equation (A 22) of the Appendix. We first estimated the Kolmogorov length scale using our spatial discretization $\mathrm{d}x = 0.592$ cm from the full reconstructed field. The Kolmogorov length scale field defined in (8.7) is presented in figure 31(*a*) phase $\varphi = 113°$ during the splash-up sequence. We choose to display this phase because the smallest values of η_k were obtained in that case. Figure 31 is a zoom of η_k in a location where the turbulence intensity level was high. Values of η_k range between 0.01 cm near the wavefront, up to 0.1 cm near the bottom and in the water column behind the wavefront, with an average value $\overline{\eta_k} = 0.028$ which is about 21 times smaller than the space resolution we used.

To avoid the contamination of the window-gathering and the associated smoothing/interpolation procedure, we calculated η_k in one single PIV window (w6, see figure 1 and table 1), which corresponds to the zoom displayed before. Calculations were done with the same spatial discretization $\mathrm{d}x = 0.592$ cm. The result is presented in figure 31(*b*). The average value in this case is $\overline{\eta_k} = 0.029$. Clearly, discrepancies are weak between the two results, except very close to the interface.

In order to evaluate the influence of the predefined space resolution on the evaluation of η_k, we made a new computation of all the velocity fields from the complete PIV image database, with a new smaller resolution: $\mathrm{d}x = 0.296$ cm. We did this for window number w6 where the seeding was particulary homogeneous and

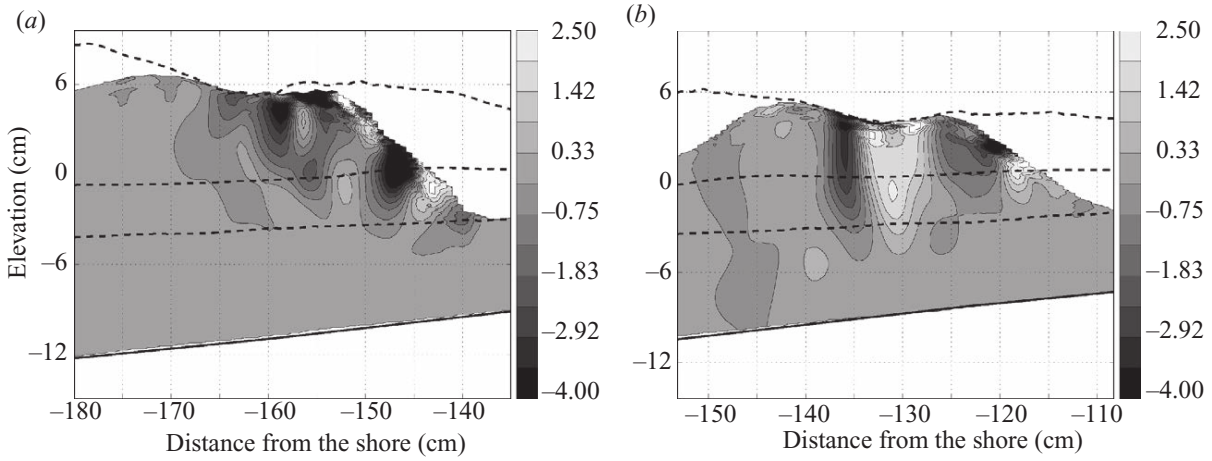

FIGURE 32. non-dimensional phase-locked 'transport-due-to-convection-term' of the fluctuating kinetic energy equation (equation (A 12) multiplied by $Tg^{-1}D^{-1}$); for (*a*) $\varphi = 106°$ and $\varphi = 176°$ (*b*).

concentrated owing to the mixing turbulence, and this configuration allowed us to decrease the elementary PIV interrogation box size up to 16×16 pixels (instead of 32×32 pixels) and to increase the overall number of velocity vectors in w6 up to 128×128 (instead of 64×64). Therefore, the spatial distribution decreased in this case to $\mathrm{d}x = 0.296$ cm. The new Kolmogorov length-scale field computed with this resolution is displayed in figure 31(*c*), and should be compared with the others. Clearly, discrepancies are small, and η_k values are similar throughout the domain, except close to the water surface for small values of the length scale ($\eta_k < 0.01$), for which, effectively, the spatial resolution is not precise enough. The average value is now $\overline{\eta_k} = 0.023$ which is very close to the previous 0.29 value, and it is about 13 times smaller than the new space resolution. For this case, the discretization seems to be good enough ($\mathrm{d}x \simeq 10\,\overline{\eta_k}$) to estimate some terms of the fluctuating energy transport equation. Unfortunately, it was not possible to use 16×16 pixels in all the windows because of the lack of particles (fewer than 5 particles in a box) in relatively deep water and in very shallow water. However, the η_k field computed with the coarse resolution $\mathrm{d}x = 0.592$ cm (figure 31*a*) looks similar to the the η_k field computed with low resolution (figure 31*c*), and we decided to calculate some terms of the fluctuating energy transport equation with our first space resolution, even if the precision is out of order near the crests.

For simplification, if we denote (U, W) the components of $\boldsymbol{U}_\varphi$, and (u, w) the components of $\boldsymbol{U}'_\varphi$, 26 different variables were computed in order to estimate the terms of the kinetic energy transport equation. These 26 terms are: $\overline{U}$, $\overline{W}$, $\overline{u^2}$, $\overline{w^2}$, $\overline{uw}$, $\partial\overline{U}/\partial x$, $\partial\overline{W}/\partial x$, $\partial\overline{U}/\partial z$, $\partial\overline{W}/\partial z$, $\partial\overline{u^2}/\partial x$, $\partial\overline{u^2}/\partial z$, $\partial\overline{w^2}/\partial x$, $\partial\overline{w^2}/\partial z$, $\partial\overline{u^3}/\partial x$, $\partial\overline{uw^2}/\partial x$, $\partial\overline{wu^2}/\partial z$, $\partial\overline{w^3}/\partial z$, $\overline{(\partial u/\partial z)(\partial w/\partial x)}$, $\overline{(\partial u/\partial z)^2}$, $\overline{(\partial w/\partial x)^2}$, $\overline{(\partial u/\partial x)^2}$, $\overline{(\partial w/\partial z)^2}$, $(\partial/\partial x)\overline{u(\partial u/\partial x)^2}$, $(\partial/\partial x)\overline{w(\partial u/\partial z)(\partial w/(\partial x)}$, $(\partial/\partial z)\overline{u(\partial w/\partial x)(\partial u/\partial z)}$, $(\partial/\partial z)\overline{w(\partial w/\partial z)^2}$. Here, the overbar represents the average over the 64 samples which have the same phase φ, as explained in § 7. The procedure of phase averaging smoothes out the fluctuations of the space-derivatives caused by the passages of eddies, but will not remove the fluctuations entirely because the successive eddies are not completely random in space and time. Evolution of the phase-averaged 'transport-due-to-convection-term', and 'production', are presented in non-dimensional form (equations (A 17) and (A 12) multiplied by $Tg^{-1}D^{-1}$) in figures 32 and 33, for phases $\varphi = 106°$ and 176°) in the vicinity of the crest. Only two phases are presented here, but we observed that transport by

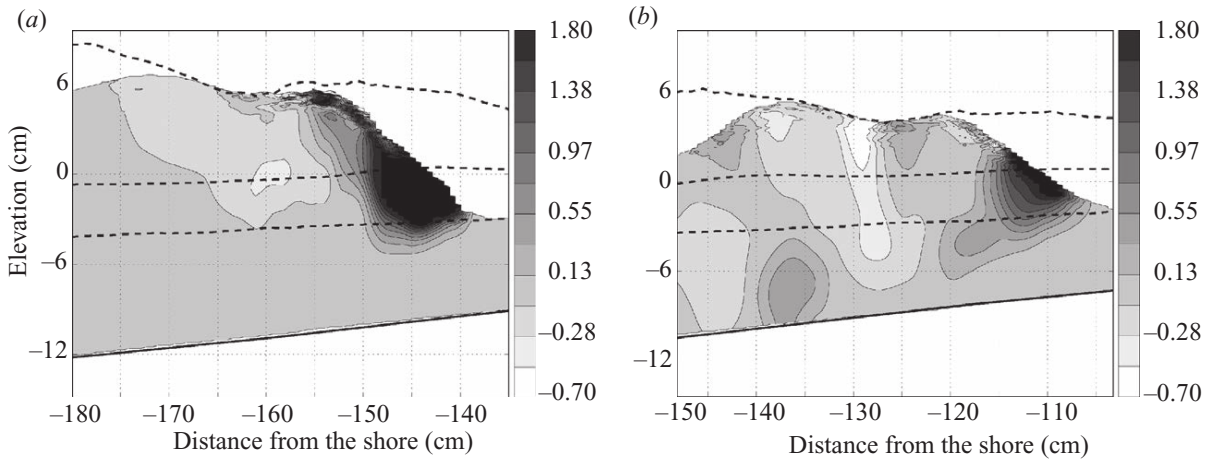

FIGURE 33. Non-dimensional phase-locked 'production-term' of the fluctuating kinetic energy equation (equation (A 17) multiplied by $Tg^{-1}D^{-1}$); for (*a*) $\varphi = 106°$ and (*b*) $\varphi = 176°$.

convection was mainly localized near the front part of the crest after the plunging event and before the last splash-up. These terms are weak under the mean sea level. In non-dimensional form, these terms are high in the swash zone, above the shoreline, because mean water depth D becomes very weak. The same remarks could be made for the transport by fluctuations (not presented here). These terms are concentrated mainly during the splash-up sequence between the second and third splash-ups; near the crest above mean sea level and very close to the surface. Non-dimensional values are also high in the swash zone.

Production terms are also localized near the crests, and more particularly near the toe of the front face of the crest, but high values last throughout the breaking event, at any phases, from the incipient breaking to the swash zone, and remain attached to the front part of the crest. Maximum non-dimensional values are always higher than unity near the toe throughout the wave propagation. As shown in Brocchini & Peregrine (2001*a*); Brocchini & Peregrine (2001*b*), fluctuating kinetic production is mainly generated in this particular location of the wave crest. Under the back face of the crest, we observed several cells of positive and negative values, but with much lower intensity than near the toe.

The viscous dissipation and diffusion terms are three orders of magnitude lower than convection or transport terms. They are not presented here. We probably did not have a high enough space resolution for the correct estimation of these terms close to the surface or to the bottom line, the elementary PIV box size being too large. Maximum non-dimensional values are in the range 0.0005 (viscous diffusion) to 0.001 (viscous dissipation). Viscous effects are higher during the bore propagating phase.

Our goal was not to present a full budget of the turbulent kinetic equation terms because (i) we did not measure the pressure terms, and (ii) we did not have everywhere the required space resolution to measure the different terms exactly. However, the few examples presented here are an illustration of the spatial repartition in the (x, z)-plane of some terms under the breaking waves.

9. Conclusions

Experiments were conducted in a 17 m long wave tank, in order to measure dynamics and kinematics of waves propagating and breaking over a 1/15 sloping beach for a particular case of a spilling–plunging breaker, with a very short first

spilling phase followed by a plunging event, a splash-up, a small second splash-up and a bore-propagating phase. PIV measurements were performed all along the swash zone on $37 \times 37\,\mathrm{cm}^2$ small windows in order to have sufficient velocity precision everywhere. We used TTL signals and wave gauge time series to synchronize all the measurements from the different small windows and merged them to obtain an instantaneous full velocity field from the incipient breaking to the wave run-up. Errors due to gathering/smoothing were estimated. We reconstructed 3264 different global velocity fields and wave profiles representing 256 different wave cycles. Ensemble-average values of velocity and transport were computed. The acquisition of 51 PIV image-couples lasted exactly 4 wave periods. So we were able to describe statistically a wave period with exactly 51 different phases. For each phase, phase-averaged values were computed by averaging the 64 instantaneous fields having the same phase. The phase-to-phase repeatability was estimated to be less than 1°. We computed instantaneous mean phase-averaged and fluctuating phase-locked data around phase-averaged values. It is the first time that phase-averaged velocities have been presented in a continuous space-domain ($U_\varphi(x, z)$) over the whole surf zone. Usually they are presented in the time-domain $U_\varphi(t)$ at some particular measurement points (x, z), and time-to-space conversion is done through the Taylor hypothesis ($x = ut$, or $\partial/\partial x = (1/u)\partial/\partial t$), which states that the temporal fluctuations could be assumed to correlate to the passage of a frozen turbulence pattern. In breaking waves, the turbulent velocities created by the large-scale motion are so large that this condition is not always satisfied. In this paper, phase averaged data and convective derivatives are computed in the whole domain without this hypothesis. Most of the terms are presented in a non-dimensional form, velocities divided by nominal phase speed $\sqrt{gD}$, and time divided by mean wave period T. The calculation of space derivatives with spline functions allowed us to compute the vorticity, and the different terms that appear in the fluctuating kinetic energy transport equation.

The envelope trough-line, which is drawn in all the figures, seems to be a natural boundary between on-shore mean velocities above this line and offshore velocities under it. Non-dimensional measured velocities are $O(1)$ near the crest-envelope, and O(0.1) under the troughs. The maximum non-dimensional value is 1.35 and occurs after the splash-up sequence. A new result is the increase of the undertow close to the bottom line during the bore-propagating phase. We observed a vertical-phase shift between velocities at the crest and velocities near the bottom, owing to friction effects and to the undertow near the bed.

We estimated the void fraction in each point of the domain by means of light-intensity image analysis and vertically integrated velocity considerations in the domain. We used light-scattering theory with a Lambert law to relate void fraction to light intensity. We found an exponential decay of void fraction with depth below the mean sea level, with a very good fit to the Hoque & Aoki (2005) semi-theoretical law. It is the first time that an ensemble-average void fraction over the whole laboratory surf zone has been measured. The air-entrainment is large during the first splash-up event with values of void fraction near 0.88 above mean sea level inside the splash-up. Then the void fraction decreases slowly when the wave propagates towards the shore, with values near 0.2–0.3. Close to the shore, aeration is still present in the front face of the wave, but also at the back face of the bore near the crest. The ensemble-average transport was evaluated with the void fraction taken into account. Results show a mean shoreward transport above the trough level and an undertow below. The maximum shoreward transport was found in the splash-up location, between the mean sea level and the trough line. The maximum seaward transport near the bottom

was found after the first splashing region when the turbulent bore is propagating towards the shore.

Several vortices with horizontal axes are generated during the breaking. The first one is generated by the plunging event. It is advected obliquely towards the bottom and moves slower than the wave crest. A second vortex is created during the splash-up phase with a vorticity amplitude greater than the first one. A third vortex is created during the second splash-up. A fourth one is generated at the front face of the propagating bore and remains attached to the bore up to the shoreline.

Plots of the phase-average fluctuating energy identify clearly the front of the breaking crest as the initiation point for kinetic energy production. Fluctuations generated at the crest spread downstream and toward the bottom. Maximum values of fluctuating kinetic energy are found during the splashing events. The fluctuating energy is transported shoreward under the wave crest by organized wave-induced flow. It is spread downward by the large eddies. Our measured values of fluctuating energy are very close, in non-dimensional form, to those measured by Govender *et al.* (2002) and Ting & Kirby (1994). Bottom shear stress has a strong local maximum in the splash-up region.

We computed the Kolmogorov length scale η_k over all the domain and found that the average η_k was about 21 times the space resolution. We have shown that for a half-space resolution the results, except near the crest interface, are very similar. So we decided to compute, with the first space resolution, the different terms that appear in the fluctuating kinetic energy propagation equation.

The dynamics of surf zone fluctuations seem to be controlled by fluctuating transport and convection of large-scale structures. Convective, fluctuating and production terms in the fluctuating kinetic transport equation are both important, more particularly inside the propagating bore during the successive splash-up cycles. Only a small portion of the wave energy loss is dissipated below the trough level. Viscous terms are relatively low, but we did not have enough space resolution, and the elementary PIV box size is too large to have a correct estimation of these terms very close to the surface or to the bottom line.

We now have a large data set of space–time evolution of the velocity field, water wave profile, and void fraction over the whole surf and swash zone. This data could be useful for testin, as a reference benchmark, numerical codes simulating breaking waves in a surf zone. By changing the slope angle and the incipient wave amplitude and period, it could be useful for studying the dynamics of spilling, strong plunging or surging breakers.

We would like to thank specifically Bertrand Zucchini for his very helpful and careful technical assistance during the study. The French National Program PATOM/IDAO and the CNRS provided part of financial support.

Appendix. Fluctuating kinetic energy equation

We use the following notation,
x is the cross-shore direction:
y is the spanwise direction,
z is the vertical upward direction,
$\boldsymbol{U}_\varphi = \overline{\boldsymbol{U}}_\varphi + \boldsymbol{U}'_\varphi$ with
$\boldsymbol{U}_\varphi = (U_\varphi, V_\varphi, W_\varphi)$, $\overline{\boldsymbol{U}}_\varphi = (\overline{U}_\varphi, \overline{V}_\varphi, \overline{W}_\varphi)$, $\boldsymbol{U}'_\varphi = (u'_\varphi, v'_\varphi, w'_\varphi)$,
pressure: $P = \overline{P} + p'$.

In the following, in order to simplify the notation, we leave the substrings φ and the primes:
$\overline{\boldsymbol{U}}_\varphi = (\overline{U}, \overline{V}, \overline{W})$, $\boldsymbol{U}'_\varphi = (u, v, w)$.
The fluctuating kinetic energy is (cf. equations (8.2) to (8.5)):

$$\overline{q^2} = \frac{(\overline{u^2} + \overline{v^2} + \overline{w^2})}{2} = \tfrac{4}{3}\,(\overline{u^2} + \overline{w^2}) \tag{A 1}$$

with:

$$\overline{v^2} = \tfrac{1}{3}\,(\overline{u^2} + \overline{w^2}). \tag{A 2}$$

The kinetic energy balance equation could be written as: (Hinze 1975)

$$\begin{aligned}\frac{\mathrm{D}}{\mathrm{D}t}\,\overline{q^2} = {} & \textit{Transport-due-to-convection} \\ & + \textit{Transport-due-to-pressure-gradient} \\ & + \textit{Transport-due-to-fluctuations} \\ & + \textit{Production} + \textit{Dissipation} + \textit{Diffusion}\end{aligned} \tag{A 3}$$

with successively in tensorial notation:
Convective transport term:

$$\textit{Transport-due-to-convection} = -\overline{U_i}\,\frac{\partial}{\partial x_i}\overline{q^2}, \tag{A 4}$$

Transport due to pressure gradient:

$$\textit{Transport-due-to-pressure-gradient} = -\frac{\partial}{\partial x_i}\overline{u_i \frac{p}{\rho}}, \tag{A 5}$$

Transport due to fluctuations:

$$\textit{Transport-due-to-fluctuations} = -\frac{\partial}{\partial x_i}\overline{u_i q^2}, \tag{A 6}$$

Production term:

$$\textit{Production} = -\overline{u_i u_j}\,\frac{\partial \overline{U_j}}{\partial x_i}, \tag{A 7}$$

Viscous dissipation term:

$$\textit{Dissipation} = -\upsilon\overline{\left(\frac{\partial u_i}{\partial x_j} + \frac{\partial u_j}{\partial x_i}\right)\frac{\partial u_j}{\partial x_i}}, \tag{A 8}$$

Viscous diffusion term:

$$\textit{Diffusion} = +\upsilon\frac{\partial}{\partial x_i}\overline{u_j\left(\frac{\partial u_i}{\partial x_j}\frac{\partial u_j}{\partial x_i}\right)}, \tag{A 9}$$

where ρ and υ are, respectively, the water density and kinematic viscosity.

A.1. *Convective transport term*

$$\begin{aligned}-\textit{Transport-due-to-convection} = \overline{U_i}\,\frac{\partial}{\partial x_i}\overline{q^2} = {} & \overline{U}\frac{\partial \overline{u^2}}{\partial x} + \overline{V}\frac{\partial \overline{u^2}}{\partial y} + \overline{W}\frac{\partial \overline{u^2}}{\partial z} + \overline{U}\frac{\partial \overline{v^2}}{\partial x} + \overline{V}\frac{\partial \overline{v^2}}{\partial y} \\ & + \overline{W}\frac{\partial \overline{v^2}}{\partial z} + \overline{U}\frac{\partial \overline{w^2}}{\partial x} + \overline{V}\frac{\partial \overline{w^2}}{\partial y} + \overline{W}\frac{\partial \overline{w^2}}{\partial z}.\end{aligned} \tag{A 10}$$

If we assume $\overline{V}=0$, then:

$$-Transport\text{-}due\text{-}to\text{-}convection = \overline{U}\frac{\partial\overline{u^2}}{\partial x}+\overline{W}\frac{\partial\overline{u^2}}{\partial z}+\overline{U}\frac{\partial\overline{v^2}}{\partial x}+\overline{W}\frac{\partial\overline{v^2}}{\partial z} + \overline{U}\frac{\partial\overline{w^2}}{\partial x}+\overline{W}\frac{\partial\overline{w^2}}{\partial z} \tag{A 11}$$

and considering (A 2), finally we have:

$$-Transport\text{-}due\text{-}to\text{-}convection = \frac{4}{3}\left(\overline{U}\frac{\partial\overline{u^2}}{\partial x}+\overline{W}\frac{\partial\overline{u^2}}{\partial z}+\overline{U}\frac{\partial\overline{w^2}}{\partial x}+\overline{W}\frac{\partial\overline{w^2}}{\partial z}\right). \tag{A 12}$$

A.2. *Fluctuating transport term*

$$-Transport\text{-}due\text{-}to\text{-}fluctuations = \frac{\partial}{\partial x_i}\overline{u_i q^2} = \frac{\partial\overline{u^3}}{\partial x}+\frac{\partial\overline{uv^2}}{\partial x}+\frac{\partial\overline{uw^2}}{\partial x}+\frac{\partial\overline{vu^2}}{\partial y}+\frac{\partial\overline{v^3}}{\partial y} + \frac{\partial\overline{vw^2}}{\partial y}+\frac{\partial\overline{wu^2}}{\partial z}+\frac{\partial\overline{wv^2}}{\partial z}+\frac{\partial\overline{w^3}}{\partial z}. \tag{A 13}$$

The gradient in the spanwise direction y of the triple correlations which involved alongshore component v could be neglected:

$$-Transport\text{-}due\text{-}to\text{-}fluctuations = \frac{\partial}{\partial x_i}\overline{u_i q^2} = \frac{\partial\overline{u^3}}{\partial x}+\frac{\partial\overline{uv^2}}{\partial x}+\frac{\partial\overline{uw^2}}{\partial x} + \frac{\partial\overline{wu^2}}{\partial z}+\frac{\partial\overline{wv^2}}{\partial z}+\frac{\partial\overline{w^3}}{\partial z}. \tag{A 14}$$

Terms with v^2 could not be measured, and as previously, we used (A 2) which gives:

$$-Transport\text{-}due\text{-}to\text{-}fluctuations = \frac{\partial}{\partial x_i}\overline{u_i q^2} = \frac{4}{3}\left(\frac{\partial\overline{u^3}}{\partial x}+\frac{\partial\overline{uw^2}}{\partial x}+\frac{\partial\overline{wu^2}}{\partial z}+\frac{\partial\overline{w^3}}{\partial z}\right). \tag{A 15}$$

A.3. *Production term*

$$-Production = \overline{u_i u_j}\frac{\partial\overline{U_j}}{\partial x_i} = \overline{u^2}\frac{\partial\overline{U}}{\partial x}+\overline{uv}\frac{\partial\overline{V}}{\partial x}+\overline{uw}\frac{\partial\overline{W}}{\partial x}+\overline{vu}\frac{\partial\overline{U}}{\partial y}+\overline{v^2}\frac{\partial\overline{V}}{\partial y} + \overline{vw}\frac{\partial\overline{W}}{\partial y}+\overline{wu}\frac{\partial\overline{U}}{\partial z}+\overline{wv}\frac{\partial\overline{V}}{\partial z}+\overline{w^2}\frac{\partial\overline{W}}{\partial z}, \tag{A 16}$$

we assume $\overline{V}=0$, so:

$$-Production = \overline{u_i u_j}\frac{\partial\overline{U_j}}{\partial x_i} = \overline{u^2}\frac{\partial\overline{U}}{\partial x}+\overline{uw}\frac{\partial\overline{W}}{\partial x}+\overline{vu}\frac{\partial\overline{U}}{\partial y}+\overline{vw}\frac{\partial\overline{W}}{\partial y}+\overline{wu}\frac{\partial\overline{U}}{\partial z}+\overline{w^2}\frac{\partial\overline{W}}{\partial z}. \tag{A 17}$$

We were not able to measure the derivative in the alongshore direction y. These regular waves are two-dimensional before breaking, with no y-variations. We assume that the terms with derivatives in the y direction are small compared to derivatives in the x cross-shore and z vertical directions (which is not the case during the last

stages of breaking). We have then:

$$-Production = \overline{u_i u_j}\frac{\partial \overline{U_j}}{\partial x_i} = \overline{u^2}\frac{\partial \overline{U}}{\partial x} + \overline{uw}\frac{\partial \overline{W}}{\partial x} + \overline{wu}\frac{\partial \overline{U}}{\partial z} + \overline{w^2}\frac{\partial \overline{W}}{\partial z}. \tag{A 18}$$

A.4. *Viscous dissipation*

Fluctuating kinetic energy dissipation is one of the most challenging parts to be estimated in the fluctuating energy equation.

$$\begin{aligned} -Dissipation = \upsilon \overline{\left(\frac{\partial u_i}{\partial x_j} + \frac{\partial u_j}{\partial x_i}\right)\frac{\partial u_j}{\partial x_i}} = \upsilon\Bigg(2\overline{\left(\frac{\partial u}{\partial y}\frac{\partial v}{\partial x}\right)} + 2\overline{\left(\frac{\partial u}{\partial z}\frac{\partial w}{\partial x}\right)} + 2\overline{\left(\frac{\partial v}{\partial z}\frac{\partial w}{\partial y}\right)} \\ + \overline{\left(\frac{\partial u}{\partial y}\right)^2} + \overline{\left(\frac{\partial u}{\partial z}\right)^2} + \overline{\left(\frac{\partial v}{\partial x}\right)^2} + \overline{\left(\frac{\partial v}{\partial z}\right)^2} + \overline{\left(\frac{\partial w}{\partial x}\right)^2} + \overline{\left(\frac{\partial w}{\partial y}\right)^2} \\ + 2\overline{\left(\frac{\partial u}{\partial x}\right)^2} + 2\overline{\left(\frac{\partial v}{\partial y}\right)^2} + 2\overline{\left(\frac{\partial w}{\partial z}\right)^2}\Bigg). \end{aligned} \tag{A 19}$$

Again, we assume that the terms with y-derivatives are small compared with other terms, so we have:

$$\begin{aligned} -Dissipation = \upsilon \overline{\left(\frac{\partial u_i}{\partial x_j} + \frac{\partial u_j}{\partial x_i}\right)\frac{\partial u_j}{\partial x_i}} = \upsilon\Bigg(2\overline{\left(\frac{\partial u}{\partial z}\frac{\partial w}{\partial x}\right)} + \overline{\left(\frac{\partial u}{\partial z}\right)^2} + \overline{\left(\frac{\partial v}{\partial x}\right)^2} + \overline{\left(\frac{\partial v}{\partial z}\right)^2} \\ + \overline{\left(\frac{\partial w}{\partial x}\right)^2} + 2\overline{\left(\frac{\partial u}{\partial x}\right)^2} + 2\overline{\left(\frac{\partial w}{\partial z}\right)^2}\Bigg). \end{aligned} \tag{A 20}$$

The two terms: $\overline{(\partial v/\partial x)^2}$ and $\overline{(\partial v/\partial z)^2}$ could not be measured with our PIV system. Using the same kind of approximation as in (A 2), we arbitrarily write:

$$\overline{\left(\frac{\partial v}{\partial x}\right)^2} = \tfrac{1}{3}\left(\overline{\left(\frac{\partial u}{\partial x}\right)^2} + \overline{\left(\frac{\partial w}{\partial x}\right)^2}\right), \tag{A 21a}$$

$$\overline{\left(\frac{\partial v}{\partial z}\right)^2} = \tfrac{1}{3}\left(\overline{\left(\frac{\partial u}{\partial z}\right)^2} + \overline{\left(\frac{\partial w}{\partial z}\right)^2}\right), \tag{A 21b}$$

so we have:

$$\begin{aligned} -Dissipation = \upsilon \overline{\left(\frac{\partial u_i}{\partial x_j} + \frac{\partial u_j}{\partial x_i}\right)\frac{\partial u_j}{\partial x_i}} = \upsilon\Bigg(2\overline{\left(\frac{\partial u}{\partial z}\frac{\partial w}{\partial x}\right)} + \frac{4}{3}\left(\overline{\left(\frac{\partial u}{\partial z}\right)^2} + \overline{\left(\frac{\partial w}{\partial x}\right)^2}\right) \\ + \frac{7}{3}\left(\overline{\left(\frac{\partial u}{\partial x}\right)^2} + \overline{\left(\frac{\partial w}{\partial z}\right)^2}\right)\Bigg). \end{aligned} \tag{A 22}$$

A.5. *Viscous diffusion*

$$\begin{aligned} Diffusion = \upsilon \frac{\partial}{\partial x_i}\overline{u_j\left(\frac{\partial u_i}{\partial x_j}\frac{\partial u_j}{\partial x_i}\right)} = \upsilon\Bigg(\frac{\partial}{\partial x}\overline{u\left(\frac{\partial u}{\partial x}\right)^2} + \frac{\partial}{\partial x}\overline{v\left(\frac{\partial u}{\partial y}\frac{\partial v}{\partial x}\right)} + \frac{\partial}{\partial x}\overline{w\left(\frac{\partial u}{\partial z}\frac{\partial w}{\partial x}\right)} \\ + \frac{\partial}{\partial y}\overline{u\left(\frac{\partial v}{\partial x}\frac{\partial u}{\partial y}\right)} + \frac{\partial}{\partial y}\overline{v\left(\frac{\partial v}{\partial y}\right)^2} + \frac{\partial}{\partial y}\overline{w\left(\frac{\partial v}{\partial z}\frac{\partial w}{\partial y}\right)} \\ + \frac{\partial}{\partial z}\overline{u\left(\frac{\partial w}{\partial x}\frac{\partial u}{\partial z}\right)} + \frac{\partial}{\partial z}\overline{v\left(\frac{\partial w}{\partial y}\frac{\partial v}{\partial z}\right)} + \frac{\partial}{\partial z}\overline{w\left(\frac{\partial w}{\partial z}\right)^2}\Bigg) \end{aligned} \tag{A 23}$$

If we remove the y-derivative, we have:

$$Diffusion = \upsilon \frac{\partial}{\partial x_i}\overline{u_j\left(\frac{\partial u_i}{\partial x_j}\frac{\partial u_j}{\partial x_i}\right)} = \upsilon\left(\frac{\partial}{\partial x}\overline{u\left(\frac{\partial u}{\partial x}\right)^2} + \frac{\partial}{\partial x}\overline{w\left(\frac{\partial u}{\partial z}\frac{\partial w}{\partial x}\right)}\right.$$
$$\left. + \frac{\partial}{\partial z}\overline{u\left(\frac{\partial w}{\partial x}\frac{\partial u}{\partial z}\right)} + \frac{\partial}{\partial z}\overline{w\left(\frac{\partial w}{\partial z}\right)^2}\right) \quad \text{(A 24)}$$

All four diffusion terms, which are the result of the derivative of triple correlation, are very low. Usually, their relative share in the total energy budget is minuscule (Piirto *et al.* 2003).

A.6. *Pressure terms*

Measuring the pressure gradient terms was beyond the capability of our experimental apparatus. The pressure term must be solved by the energy balance by summing up the other terms.

A.7. *Conclusions*

Twenty-six different terms must be estimated to yield equations (A 12), (A 15), (A 17), (A 22) and (A 24). These terms are

$$\overline{U}, \overline{W}, \overline{u^2}, \overline{w^2}, \overline{uw}, \partial\overline{U}/\partial x, \partial\overline{W}/\partial x, \partial\overline{U}/\partial z, \partial\overline{W}/\partial z, \partial\overline{u^2}/\partial x, \partial\overline{u^2}/\partial z, \partial\overline{w^2}/\partial x,$$
$$\partial\overline{w^2}/\partial z, \partial\overline{u^3}/\partial x, \partial\overline{uw^2}/\partial x, \partial\overline{wu^2}/\partial z, \partial\overline{w^3}/\partial z, \overline{(\partial u/\partial z\partial w/\partial x)}, \overline{(\partial u/\partial z)^2}, \overline{(\partial w/\partial x)^2},$$
$$\overline{(\partial u/\partial x)^2}, \overline{(\partial w/\partial z)^2}, \partial/\partial x\overline{u(\partial u/\partial x)^2}, \partial/\partial x\overline{w(\partial u/\partial z\partial w/\partial x)}, \partial/\partial z\overline{u(\partial w/\partial x\partial u/\partial z)},$$
$$\partial/\partial z\overline{w(\partial w/\partial z)^2}.$$

REFERENCES

Adrian, R. J. 1991 Particle-imaging techniques for experimental fluid mechanics. *Annu. Rev. Fluid Mech.* **23**, 261–304.

Basco, D. R. 1985 A qualitative description of wave breaking. *J. Waterway Port Coastal Ocean Engng* **111**, 171–188.

Battjes, A. 1988 Surf-zone dynamics. *Annu. Rev. Fluid Mech.* **20**, 257–293.

Blenkinsopp, C. E. & Chaplin, J. R. 2005 Measurement of air–water interfaces in plunging breaking waves. *Proc. 20th WWWFB International Workshop on Water Waves and Floating boadies, Longyearbyen, Norway* (ed. J. Grue), vol. 1, pp. 27–30.

Bonmarin, P. 1989 Geometric properties of deep water breaking waves. *J. Fluid Mech.* **209**, 405–433.

Brocchini, M. & Peregrine, D. H. 2001*a* The dynamics of strong turbulence at free surface. Part 1. Description. *J. Fluid Mech.* **449**, 225–254.

Brocchini, M. & Peregrine, D. H. 2001*b* The dynamics of strong turbulence at free surface. Part 2. Free-surface boundary conditions. *J. Fluid Mech.* **449**, 255–290.

Chang, K. A., Hsu, T. J. & Liu, P. L. 2001 Vortex generation and evolution in water waves propagating over a submerged rectangular obstacle: Part I, solitary waves. *Coastal Engng* **44**, 13–36.

Chang, K. A., Hsu, T. J. & Liu, P. L. 2005 Vortex generation and evolution in water waves propagating over a submerged rectangular obstacle: Part II, cnoidal waves. *Coastal Engng* **52**, 257–283.

Chang, K. A. & Liu, P. L. 1998 Velocity, acceleration and vertical vortex under a breaking wave. *Phys. Fluids* **10**, 327–329.

Chang, K. A. & Liu, P. L. 1999 Experimental investigation of turbulence generated by breaking waves in water of intermediaite depth. *Phys. Fluids* **11**, 3390–3400.

Chanson, H., Aoki, S. & Maruyama, M. 2002 Unsteady air bubble entrainment and detrainment at a plunging breaker dominant time scales and similarity of water level variations. *Coastal Engng* **46**, 139–157.

Christensen, E. D., Walstra, D. J. & Emerat, N. 2002 Vertical variation of the flow across the surf zone. *Coastal Engng* **45**, 169–198.

Cohn, R. K. & Koochesfahani, M. M. 2000 The accuracy of remapping irregularly spaced velocity data onto a regular grid and the computation of vorticity. *Exps. Fluids* Suppl., S61–S69.

Conley, D. C. & Inman, D. L. 1992 Field observations of the fluid granular boundary layer under near breaking waves. *J. Geophys. Res.* **97**, 9631–9643.

Cowen, E. A. & Monismith, S. G. 1997 A hybrid digital particle tracking velocimetry technique. *Exps. Fluids* **22**, 199–211.

Cowen, E. A., Sou, I. M., Liu, L. F. & Raubenheimer, B. 2003 PIV measurements within a laboratory generated swash zone. *J. Engng Mech.* **129**, 1119–1129.

Cox, D. T. & Anderson, S. L. 2001 Statistics of intermittent surf zone turbulence and observations of large eddies using PIV. *Coastal Engng* **43** (2), 121–131.

Cox, D. T. & Kobayashi, N. 1997 A kinematic undertow model with a logarithmic boundary layer. *J. Waterway Port Coastal Ocean Engng* **123**, 354–360.

Cox, D. T. & Kobayashi, N. 2000 Identification of intense intermittent coherent motions under shoaling and breaking waves. *J. Geophys. Res.* **105**, 14 223–14 236.

Cox, D. T. & Shin, S. 2003 Laboratory measurements of void fraction and turbulence in the bore region of surf zone waves. *J. Engng Mech.* **129**, 1197–1205.

Cox, D., Kobayashi, N. & Koyabasu, A. 1995 Experimental and numerical modeling of surf zone hydrodynamics. *CACR Tech. Rep.*

Dabiri, D. & Gharib, M. 1997 Experimental investigation of the vorticity generation within a spilling water wave. *J. Fluid Mech.* **330**, 113–139.

Dancey, C. L. & Diplas, P. 2003 *The Probability of Sediment Movement at the Threshold of Motion and Time Dependent Fluid Processes*. San Diego Tech. Book, Albert Gyr.

De Boor, C. 1978 *A Practical Guide to Splines*. Springer. (Revised edition 2001).

De Serio, F. & Mossa, M. 2006 Experimental study on the hydrodynamics of regular breaking waves. *Coastal Engng* **53**, 99–113.

Efron, B. & Tibshirani, R. 1993 *An Introduction to the Bootstrap*. Chapman & Hall.

Fenton, J. D. 1985 A 5th-order Stokes theory for steady waves. *J. Waterway Port Coastal Ocean Engng* **111**, 216–233.

Fouras, A. & Soria, J. 1999 Accuracy of out of plane vorticity measurements from in-plane velocity field data. *Exps. Fluids* **22**, 409–430.

George, R., Flick, R. E. & Guza, R. T. 1994 Observations of turbulence in the surf zone. *J. Geophys. Res.* **99**, 801–810.

Govender, K. 1999 Velocity, vorticity and turbulence measurements in the surf zone. PhD thesis, University of Natal, Durban.

Govender, K., Mocke, G. P. & Alport, M. J. 2002 Video-imaged surf zone and roller structures and flow fields. *J. Geophys. Res.* **107**, X1–X21.

Hattori, M. & Aona, T. 1985 Experimental study on turbulence structures under breaking waves. *Coastal Eng. Japan* **28**, 97–116.

Hinze, J. 1975 *Turbulence*, 2nd edn. McGraw–Hill.

Hoque, A. & Aoki, S. 2005 Distributions of void fraction under breaking waves in the surf zone. *Ocean Engng* **32**, 1829–1840.

Jansen, P. C. 1986 Laboratory observation of the kinematics in the aerated region of breaking waves. *Coastal Engng* **9**, 453–477.

Kimmoun, O., Branger, H. & Zucchini, Z. 2004 Laboratory PIV measurements of wave breaking on a beach. *Proc. ISOPE Meeting, Toulon, France* **VR202**, pp. 1–6.

Lamarre, E. & Melville, W. K. 1991 Air-entrainment and dissipation in breaking waves. *Nature* **351**, 469–451.

Lamarre, E. & Melville, W. K. 1994 Void fraction measurements and sound speed fields in bubble plumes generated by breaking waves. *J. Acoust. Soc. Am.* **95**, 1317–1328.

Lin, J. C. & Rockwell, D. 1994 Instantaneous structure of a breaking wave. *Phys. Fluids* **6** (9), 2877–2879.

Lin, J. C. & Rockwell, D. 1995 Evolution of a quasi-steady breaking wave. *J. Fluid Mech.* **302**, 29–43.

Loewen, M. R. & Melville, W. K. 1994 An experimental investigation of the oscillations of bubble plumes entrained by breaking waves. *J. Acoust. Soc.* **96** (3), 1329–1343.

Longo, S. 2003 Turbulence under spilling breakers unsing discrete wavelets. *Exps. Fluids* **34**, 181–191.

Lubin, P., Vincent, S., Abadie, S. & Caltagirone, J. P. 2006 Three-dimensional large eddy simulation of air entrainment under plunging breaking waves. *Coastal Engng* **53**, 631–655.

Madsen, P. A., Sovensen, O. R. & Shaffer, H. A. 1997 Surf-zone dynamics simulated by a Boussinesq type model. *Coastal Engng* **32**, 255–319.

Melville, W. K., Veron, F. & White, C. J. 2002 The velocity field under breaking waves: coherent structures and turbulence. *J. Fluid Mech.* **454**, 203–233.

Meunier, P. & Leweke, T. 2003 Analysis and treatment of errors due to high velocity gradients in particle image velocimetry. *Exps. Fluids* **35**, 408–421.

Miche, R. 1951 Le pouvoir réfléchissant des ouvrages maritimes exposés à l'action de la houle. *Ann. Ponts Chaussées* **121**, 285–319.

Misra, S., Kirby, J. T., Brocchini, M., Veron, F. & Thomas, M. 2005 Coherent turbulent structures in a quasi-steady spilling breaker. *Proc. Waves 05, Fifth Intl Symp. on Ocean Wave Measurements and Analysis, Madrid*, pp. 1–10.

Mocke, G. 2001 Structure and modeling of surf zone turbulence due to wave breaking. *J. Geophys. Res.* **106** (C8), 17 039–17 057.

Nadaoka, K., Kino, M. & Koyano, Y. 1989 Structure of turbulent flow field under breaking waves in the surf zone. *J. Fluid Mech.* **204**, 359–387.

Peirson, W. L. 1997 Measurement of surface velocities and shears at a wavy air–water interface using particle image velocimetry. *Phys. Fluids* **23**, 427–437.

Peregrine, D. H. 1983 Breaking waves on beaches. *Annu. Rev. Fluid Mech.* **15**, 149–178.

Peregrine, D. H. & Svendsen, I. A. 1978 Spilling breakers, bores and hydraulic jumps. In *Proc. 16th Intl Conf. Coastal Engng ASCE*, vol. 16, pp. 540–550.

Perlin, M., Bernal, L. & He, J. 1996 An experimental study of deep water plunging breakers. *Phys. Fluids* **8** (9), 2365–2374.

Petti, M. & Longo, S. 2001 Turbulence experiments in the swash zone. *Coastal Engng* **43**, 1–24.

Piirto, M., Saaranrine, P., Eloranta, H. & Karvinen, R. 2003 Measuring turbulence energy with PIV in a backward-facing step flow. *Exps. Fluids* **35**, 219–236.

Shamoun, B., El Beshbeeshy, M. & Bonazza, R. 1999 Light extinction technique for void fraction measurements in bubbly flow. *Exps. Fluids* **26**, 16–26.

Skyner, D. 1996 A comparison of numerical and experimental measurements of the internal kinematics of a deep-water plunging wave. *J. Fluid Mech.* **315**, 51–64.

Spedding, G. R. & Rignot, E. J. 1993 Performance analysis and application of grid interpolation techniques for fluid flows. *Exps. Fluids* **15**, 417–430.

Stansby, P. K. & Feng, T. 2005 Kinematics and depth integrated terms in surf zone waves from laboratory measurement. *J. Fluid Mech.* **529**, 279–310.

Stanton, T. P. & Thornon, E. B. 2000 Profiles of void fraction and turbulent dissipation under breaking waves in the surf zone. In *Proc. 27th Intl Conf. Coastal Engng ICCE*, vol. 1, pp. 70–79.

Svendsen, I. A. 1987 Analysis of surf zone turbulence. *J. Geophys. Res.* **92**, 5115–5124.

Ting, F. C. & Kirby, J. T. 1994 Observation of undertow and turbulence in a laboratory surf zone. *Coastal Engng* **24**, 51–80.

Ting, F. C. & Kirby, J. T. 1995 Dynamics of surf zone turbulence in a strong plunging breaker. *Coastal Engng* **24**, 177–204.

Ting, F. C. & Kirby, J. T. 1996 Dynamics of surf zone turbulence in a spilling breaker. *Coastal Engng* **27**, 131–160.

Ting, F. C. K. 2001 Laboratory study of wave and turbulence velocities in a broad-banded irregular wave surf zone. *Coastal Engng* **43**, 183–208.

Trowbridge, J. & Elgar, S. 2001 Turbulence measurements in the surf zone. *J. Phys. Oceanogr.* **31**, 2403–2417.

Westerweel, J. 1993 Digital Particle Image Velocimetry. PhD thesis. Delft University Press.

Westerweel, J. 1994 Efficient detection of spurious vectors in particle image velocimetry data. *Exps. Fluids* **16**, 236–247.

Westerweel, J., Daribi, D. & Gharib, M. 1997 The effect of a discrete window offset on the accuracy of cross-correlation analysis of digital PIV recordings. *Exps. Fluids* **23**, 20–28.

Wu, J. 1988 Bubbles in the near surface ocean: a general description. *J. Geophys. Res.* **93**, 587–590.

Zoubir, A. M. & Boashash, B. 1998 The bootstrap and its application in signal processing. *IEEE Signal Process. Mag.* **15** (1), 55–76.